Designer Phospholipid Capping Ligands for Soft Metal Halide Nanocrystals

Working Paper

Author(s):
Morad, Viktoriia; Stelmakh, Andriy; Svyrydenko, Mariia; Feld, Leon G.; Boehme, Simon C.; Aebli, Marcel; Affolter, Joel; Kaul, Christoph J.; Schrenker, Nadine J.; Bals, Sara; Sahin, Yesim; Dirin, Dmitry N.; Cherniukh, Ihor; Raino, Gabriele; Baumketner, Andrij; Kovalenko, Maksym V.

Publication date:
2023-11-13

Permanent link:
https://doi.org/10.3929/ethz-b-000650625

Originally published in:
Research Square, https://doi.org/10.21203/rs.3.rs-3595876/v1

Funding acknowledgement:
180544 - NCCR Catalysis (phase I) (SNF)

Designer Phospholipid Capping Ligands for Soft Metal Halide Nanocrystals

Viktoriia Morad
ETH Zurich https://orcid.org/0000-0002-9712-0433
Andriy Stelmakh
ETH Zurich https://orcid.org/0000-0002-6898-1816
Mariia Svyrydenko
ETH Zurich https://orcid.org/0009-0003-7035-9684
Leon G. Feld
ETH Zurich https://orcid.org/0000-0001-9755-5085
Simon C. Boehme
ETH Zurich https://orcid.org/0000-0002-8399-5773
Marcel Aebli
Joel Affolter
Christoph J. Kaul
Nadine J. Schrenker
Sara Bals
Yesim Sahin
Dmitry N. Dirin
Ihor Cherniukh
Gabriele Raino
Andrij Baumketner
Institute for Condensed Matter Physics https://orcid.org/0000-0003-2726-931X
Maksym V. Kovalenko (mvkovalenko@ethz.ch)
ETH Zurich https://orcid.org/0000-0002-6396-8938

Research Article

Keywords:

Posted Date: November 14th, 2023

DOI: https://doi.org/10.21203/rs.3.rs-3595876/v1

Designer Phospholipid Capping Ligands for Soft Metal Halide Nanocrystals

Viktoriia Morad[1,2], Andriy Stelmakh[1,2], Mariia Svyrydenko[1,2], Leon G. Feld[1,2], Simon C. Boehme,[1,2] Marcel Aebli[1,2], Joel Affolter[1], Christoph J. Kaul[1], Nadine J. Schrenker[3], Sara Bals[3], Yesim Sahin,[1,2] Dmitry N. Dirin,[1,2] Ihor Cherniukh[1,2], Gabriele Raino[1,2], Andrij Baumketner[4] & Maksym V. Kovalenko[1,2]*

[1]Department of Chemistry and Applied Biosciences, Institute of Inorganic Chemistry, ETH Zürich,

Zürich, Switzerland

[2]Empa – Swiss Federal Laboratories for Materials Science and Technology, Dübendorf, Switzerland

[3]Electron Microscopy for Materials Science (EMAT) and NANOlab Center of Excellence, University of Antwerp, Antwerp, Belgium

[4]Institute for Condensed Matter Physics, National Academy of Sciences of Ukraine, Lviv, Ukraine

The success of colloidal semiconductor nanocrystals (NCs) in science and optoelectronics is inextricable from their surfaces. The functionalization of lead halide perovskite (LHP) NCs[1-5] poses a formidable challenge due to their structural lability, unlike the well-established covalent ligand-capping of conventional semiconductor NCs[6,7]. We posited that the vast and facile molecular engineering of phospholipids as zwitterionic surfactants can deliver highly customized surface chemistries for metal halide NCs. Molecular dynamics simulations inferred that ligand-NC surface affinity is primarily governed by the structure of the zwitterionic headgroup, particularly by the geometric fitness of the anionic and cationic moieties into the surface lattice sites, as corroborated by the NMR and FTIR data. Lattice-matched primary-ammonium phospholipids enhance the structural and colloidal integrity of hybrid organic-inorganic LHPs ($FAPbBr_3$ and $MAPbBr_3$, FA-formamidinium; MA-methylammonium) and lead-free metal halide NCs. The molecular structure of the organic ligand tail governs the long-term colloidal stability and compatibility with solvents of diverse polarity, from hydrocarbons to acetone and alcohols. These NCs exhibit photoluminescence quantum yield (PL QY) above 96% in solution and solids and minimal PL intermittency at the single particle level with an average ON fraction as high as 94%, as well as bright and high-purity (ca. 95%) single-photon emission.

LHP NCs, of the general formula $APbX_3$ (A = Cs, MA, FA; X=Cl, Br, I), receive immense scientific and practical interest as narrow band emitters for displays or as quantum light sources[8-13], whereas other metal halides (**Fig. 1a**) are pursued as broadband emitters for solid-state lighting, scintillation, and thermometry[14-16]. An imminent challenge impeding the progress in the chemistry and applications of many metal chloride, bromide, and iodide NCs is that strongly binding ligands readily outcompete the relatively low internal lattice energy.[17] For instance, typical anionic and cationic surfactants that attach to halide NC surfaces in an ionic manner, displacing surface ions with the ligand head groups (**Fig. 1b**)[4,18-20], also readily engage in adverse solubilization equilibria with the ions constituting the inorganic NC cores (**Fig. 1c**). This problem culminates with hybrid organic-inorganic perovskite compositions – $MAPbX_3$ and $FAPbX_3$ NCs. We hypothesized that zwitterionic, hence charge-neutral, capping molecules offer a general mitigation strategy for avoiding these adverse ionic metathesis reactions with NC cores, as motivated by our recent work on $CsPbBr_3$ NCs with several commercial long-chain zwitterions (phosphocholines, **Fig. 1d**, γ-amino acids, and sulfobetaines)[21-23]. Herein, we sought to design and implement a library of phospholipid capping ligands (**Fig. 1e**) to broaden the compositional scope of metal halides available in the form of finely engineered NCs. Notably, only through this approach were we able to produce surface-robust, highly emissive $MAPbX_3$ and $FAPbX_3$ NCs. The zwitterionic group engineering was computationally guided by assessing ligand-surface binding with molecular dynamics (MD) simulations. Solid-state NMR and FTIR spectroscopy then corroborated the atomistic models. Our design of chemically pure phospholipids with various head, bridge, and tail groups leverages facile synthesis methods developed over the last decades[24-30]. The utility of the entire library of ligands was assayed through post-synthetic anchoring to the NC surfaces. The vast molecular engineering of phospholipids endowed the compatibility of ligand-capped NCs with solvents of diverse polarity, ranging from hydrocarbons to alcohols, and enhanced luminescent properties in thin films and at the single particle level.

Determining the binding mode of zwitterionic ligands

Empirically, we have seen the efficacy of commercial long-chain zwitterions as ligands for $CsPbX_3$ NCs[21-23,31], chiefly $CsPbBr_3$. A champion ligand was natural lecithin (a physiological mixture of glycerophospholipids with quaternary and primary ammonium moieties), affording robust $CsPbBr_3$ colloids down to small NC sizes

of 3 nm. Further progress towards customizable phospholipid ligands for the entire family of LHP NCs and beyond requires a concerted computational and experimental effort to rationalize the binding of phospholipids at the molecular level. We first set to find whether both charged groups of the ligand participate in anchoring to the NC surface. We employed a combination of classical MD simulations, FTIR spectroscopy and Rotational-Echo Double-Resonance (REDOR) NMR spectroscopy. The surface of the NCs was modeled with a slab of bulk cubic $FAPbBr_3$, terminated with FABr-rich (100) crystallographic planes (see **Supplementary Note 1**). One alkyl phosphocholine (PC) ligand was placed at 0.5 nm above the surface, and the system was solvated with toluene. During equilibration, the ligand quickly adsorbs onto the surface, assuming a conformation which is further referred to as binding mode 1 (BM1**, Fig. 2a**). We anticipated that the ligand might also displace some of the native ions from the surface similar to oleylammonium binding to the surface of $CsPbBr_3$ NCs[20]. Thus, three possibilities – displacement of FA (BM2), bromide (BM2'), or both FA and bromide (BM3) – are depicted in **Fig. 2a**. A replica-exchange[32,33] MD simulation is then used to explore the basic binding modes and to determine which of them has the lowest free energy at room temperature (see **Methods** and **Supplementary Notes 1-2**, as well as **Extended Data Fig. 1**). The population of the starting BM1 diminishes as the simulation progresses, whereas BM3 dominates the ensemble in the late stages of the simulation (**Fig. 2b**). Similar results for $CsPbBr_3$ surfaces indicate that A cation and the slight difference in the crystal structure do not play a significant role (**Extended Data Fig. 2**). Furthermore, BM3 prevails also at other surface stoichiometries, with the FABr and ligand concentrations between 0 and 1 per binding site (see **Extended Data Fig. 3**). Attachment of the PC ligand to $FAPbBr_3$ and $CsPbBr_3$ NCs through the phosphate group binding to the surface Pb atoms is attested with ^{31}P-^{207}Pb REDOR NMR (**Fig. 2c,** see **Methods** and **Supplementary Fig. 7-8** for details) and by the FTIR spectroscopy (**Fig. 2d**, **Supplementary Note 3, Supplementary Figs. 9-12**). Notably, MD simulations suggest that the relatively bulky trimethylammonium head group of the bound ligand is elevated by ≈0.15 nm as compared to the surface FA cations (**Fig. 3a, Supplementary Table 1**). Therefore, we have investigated whether the surface can sustain an ever-increasing degree of FABr substitution by the PC ligand. The complete surface stability map as a function of ligand and FABr concentrations relative to the maximum possible surface

coverage is presented in **Extended Data Fig. 4**. Although a stable surface is still observed at 50% FABr substitution, a small fraction of PC ligands, as well as FA and Br ions, do not participate in surface passivation (**Fig. 3c**, **Extended Data Fig. 3c**). Further increase of [ligand]/[FABr] ratio leads to a complete rupture of the PbBr underlayer (**Fig. 3e**), suggesting that achieving higher than 50% surface coverage with the PC ligand is unlikely.

Tailoring the head-group affinity

Rethinking the cationic moiety was a significant leap in the project. Compared to the PC, an analogous zwitterionic head group with primary ammonium moiety (instead of fully methylated), namely phosphoethanolamine (PEA), allows for an excellent geometric fit on A-site (**Fig. 3a,b**) and theoretically allows up to 100% surface coverage (**Fig. 3d,f**). The absence of structural degradation or ligand desorption in simulations (**Fig. 3d,f, Extended Data Fig. 3 and 4**) hints that PEA is better suited for passivating $FAPbBr_3$ NC under otherwise identical conditions. We also note that primary ammonium ligands, such as oleylammmonium (OAm), had been the first ligand kind used for producing monodisperse $CsPbBr_3$ and $FAPbBr_3$ LHP NCs[1,2] and were shown to strongly bind to the surface A-site pockets (**Fig. 1b**)[20,34,35]. At the same time, such cationic-ligand binding was proven highly labile owing to the acid-base equilibrium with the neutral primary amine, seen as a rapid loss of ligands and, consequently, the NC integrity upon repetitive purification of NCs[34].

The computational design was put to test by synthesizing $FAPbBr_3$, as well as $CsPbBr_3$ and $MAPbBr_3$ NCs, capped with both PC and PEA ligands. We used the TOPO/$PbBr_2$ room-temperature synthesis method to form these NCs[31], followed by the post-synthetic displacement of weakly bound trialkylphosphine oxide and alkylphosphinic acid ligands with the ligand of choice (phospholipids), and subsequent isolation and purification of NCs (see **Methods** and **Extended Data Fig. 5a,b**). PEA-ligand binding through the phosphate-group coordination to lead atoms along with the ammonium-group insertion on the surface A-site (BM3 in **Fig. 2a**) is confirmed by the FTIR and ^{31}P-^{207}Pb REDOR NMR spectroscopies (**Supplementary Figs. 8-12**). Interestingly, when comparing NCs capped with these ligands, initially stable hexadecyl-PC-capped $FAPbBr_3$ NCs lose colloidal stability already after several days, while monodisperse hexadecyl-PEA-capped NCs of the same size remain stable in colloids for months (**Fig. 3g-i, Supplementary Table 13**). Furthermore, $MAPbBr_3$

and $CsPbBr_3$ NCs exhibited an even stronger drop in colloidal stability with hexadecyl-PC-ligand (compared to PEA-analogue, **Extended Data Fig. 5c**).

Ligand tail engineering

The apparent colloidal stability is a combined effect of the binding group affinity to the NC surface and the structure of the ligand tail. For instance, single hydrocarbon tails (such as hexadecyl) tend to form crystalline domains and are inferior to more entropic tails comprising bent oleyl or branched hydrocarbons[36] in instilling efficient steric repulsion. Unsurprising was thus to observe the efficacy of the ligand in which the PC-head group is paired with the dioleyl-glycerophosphate fragment and, likewise, in natural lecithin comprising diverse long-chain fatty acid substituents[21,37]. Besides suited steric repulsion, the ligand shall yield long-term colloidal stability when the binding strength outcompetes the solvation-induced desorption of the ligand. For a given "good" tail, transitioning from PC to PEA head group afforded a two-fold increase in the estimated surface coverage (by NMR) and robust purification through multiple cycles of precipitation with a non-solvent, retaining uniform size and shape (**Extended Data Fig. 5d**).

We thus set out to synthesize and test a library of PEA-based capping molecules, reasoning that anchoring tail groups (R) of aliphatic, aromatic, halogenated, or polyether structures (**Extended Data Fig. 6a**) will render the resulting NCs dispersible in a broad range of common organic solvents. Synthesis of PC-terminated phospholipids with aliphatic chains enjoys extended prior art with a multitude of optimized reactions[30], owing to the prevalence of PC-lipids in biological membranes[38] and their broad use for engineering liposomes for medical applications (*e.,g.* drug or gene delivery)[24,39,40] or as drugs on their own[41,42]. We first find that hexadecyl-PEA can be conveniently isolated by adopting the synthesis of hexadecyl-PC from hexadecanol by Engels *et al.*[29], skipping the last methylation step. We then generalized this synthesis approach for various alcohols (ROH), converting them into preparative quantities of the respective R-PEA ligands beginning with $POCl_3$ in three steps (**Fig. 4a**). The first two steps of gradual Cl exchange are one-pot reactions to form oxazaphospholane cycle, following with acidic hydrolysis (**Methods**).

Each of the tested ligand tails attached to a single PEA head group (21 in total; **Extended Data Fig. 6a**) imparted long-term colloidal stability of LHP NCs in specific solvents, echoing the "like dissolves the like" principle (**Fig. 4b**). For the respective ligand-solvent pairs, also the purification methodology needs to be

adjusted, particularly the selection of the antisolvent (**Supplementary Note 6** and **Supplementary Tables 11-12**). A branched aliphatic tail (-C8C12) is best compatible with aliphatic hydrocarbon solvents, whereas phenyl- or halide-terminated tails render LHP NCs preferentially dispersible in, respectively, aromatic or halogenated solvents (**Fig. 4c-e, Supplementary Fig. 19**). Dispersing LHP NCs in common polar solvents, such as acetone, alcohols or acetylacetone, without compromising their morphology, had thus far remained a formidable challenge. The matter is resolved in this study using PEA-ligands with poly(ethylene) glycol (PEG) and poly(propylene) glycol (PPG) tails (-PEG-OMe, -Solutol (-PEG-OH), and -PPG-OH), all affording long-term colloidal stability, retaining monodispersity and cuboid shape, as well as high emissivity (**Fig. 4f-g**, **Supplementary Figs. 20-22**). For instance, PPG-PEA, unlike to apolar aliphatic ligands (i.e. lecithin), renders $FAPbBr_3$ and $CsPbBr_3$ NCs highly dispersible (up to 67% by weight, inorganic basis) in PGMEA (propylene glycol methyl ether acetate, **Figure 4h**, **Supplementary Fig. 23**), an environmentally benign solvent of broad use in optoelectronics, particularly for formulating quantum dot (QD) inks in manufacturing displays.[43,44] Another exciting avenue lies in the ability to fine-tune the inter-NC separation in NC solids, as routinely accomplished for self-assembled NC superlattices[10,45,46]. We thus have devised stable colloids with polystyrene-PEA ligands synthesized from commercial OH-terminated polystyrenes of adjustable molecular weight (0.93-21 kDa). Rigid polystyrene tails increase the inter-NC spacing to at least 5 nm in NC monolayers (**Fig. 4i-k**), as compared to 1.2 nm with C8C12-PEA-capping. Inexpensive LHP NCs are of growing interest also as photocatalysts in organic synthesis, owing to reduced carrier trapping and optical tunability;[47] yet the studies have been stalled by the lability of LHP NCs in common polar, green solvents - alcohols and ethers. PPG-PEA-ligand is an enticing ligand choice for feasibility studies, as it imparts robustness to $CsPbBr_3$ NC colloids in diverse organic solvents. We conducted reductive C-C bond coupling with benzyl bromide as a substrate, previously reported with $CsPbBr_3$ perovskite NCs[48] but not with common Ir-based photocatalysts. A drastic increase in the product yield (in %) was reached upon transitioning from toluene (29%) to n-butanol (99%), for a reaction run time of 4h at 0.4 mol% of catalyst (**Extended Data Fig. 7**). Lecithin-capped QDs, dispersable in hexane and toluene only, reached a product yield of just 16% and 22%, respectively.

Light-emissivity of alkyl-PEA-capped $APbBr_3$ NCs

TOPO/$PbBr_2$ synthesis[31] coupled with subsequent PEA-ligand-capping affords highly robust colloids of

$FAPbBr_3$ and $MAPbBr_3$ QDs (NC sizes down to just a few nm), and thus their closer, much-awaited exploration at an ensemble and single-particle levels and comparison with thoroughly studied $CsPbBr_3$ NCs. For instance, C8C12-PEA-capped 6-nm $FAPbBr_3$ NCs exhibit unaltered optical properties after ten rounds of purification (**Supplementary Fig. 25**)**.** $MAPbBr_3$ NCs (10 nm) display similar stability (**Supplementary Fig. 26**). Compact, spin-coated films of C8C12-PEA-capped $FAPbBr_3$ NCs exhibit room-temperature PLQYs of 96-97% (5.5-12 nm size range, 500-525 nm PL peak range; **Fig. 5a, Supplementary Figs. 29-30**). The measured PL QY value is retained when altering the optical density (film thickness, **Fig. 5b**) by *ca*. an order of magnitude, attesting inherent near-unity PL quantum efficiency. Both PL QY and PL peak wavelengths of colloids and films sustain at least three months of storage under ambient conditions without encapsulation (**Fig. 5c**).

Not only do purified C8C12-PEA-capped NCs exhibit higher PL QY, compared to PC and OAm ligands, but they also retain their emissivity upon dramatic dilution of the solution (up to 1000-fold in **Fig. 5d**). Far more diluted samples ($\times 10^4$-10^5) are required for preparing samples for single-particle spectroscopy in conventional micro-PL setups. Detrimental processes – ligand desorption, which caused NC aggregation, and chemical reactivity towards trace water and oxygen or even the polymer used as a matrix - are drastically aggravated upon extreme dilution. Structurally labile $CsPbBr_3$ NCs were reported to shrink in size, alter their morphology and surface composition, and photobleach[49,50]. Fluorescence blinking – stochastic switching between bright ON and dim OFF states are universally observed in almost all quantum emitters at room temperature. Blinking is commonly attributed to the trapping of charges on surface defects upon photoexcitation, and along with PL intensity of single NCs, serves as a diagnostics of the surface electronic state. Single-dot PL data (**Fig. 5e-i**) evidence a profound role played by the capping ligand in achieving spectrally stable PL, suppressed blinking (94% "ON" state), as well as high single-photon purity with $g^2(0)$ down to 0.055 from single C8C12-PEA-capped $FAPbBr_3$ NCs. We note that achieving nearly blinking-free emission from CdSe-based NCs required epitaxial overgrowth with minimally strained lattice-matched wider-band gap material[51-53]. For comparison, the average outcome from single OAm-capped $FAPbBr_3$ NCs, which are minimally purified to reduce ligand desorption, is 73% of the time in the bright state and overall brightness of only 20-30% of the PEA-coated counterparts. These significant differences in favor of PEA-ligated NCs, as well as the narrower dispersion of PL characteristics, are echoed by statistics over a total of 78 QDs (**Supplementary Fig. 30**). Analogous improvements have been realized also for $CsPbBr_3$ and $MAPbBr_3$ NCs (**Extended Data Fig. 8**). We note that

single PEA-cappedFAPbBr$_3$ NCs also greatly outperform NCs capped with commercial lecithin **(Supplementary Figs. 31-33**). Notably, single PEA-capped QDs retain high brightness (ca. 3 x 10^5 cps) and high ON fraction (ca. 90%) beyond one hour of continuous operation (Supplementary Fig. 33b and 33c).

Broader implications of phospholipid ligand capping

Thus far, we comprehensively presented the design of phospholipid ligation for one compositional family of LHP NCs (APbBr$_3$; A=Cs, FA, MA) and a single binding head group (PEA), validated computationally and through solid-state NMR, and then synthetically paired with 21 structurally different tail groups. A far broader deployment of phospholipids as capping ligands is anticipated from the feasibility studies. For instance, adjusting the spacing between the ammonium and phosphate groups aids in matching the larger lattice constant, illustrated for iodide-rich LHP NCs (**Extended Data Fig. 9**), which are stable with phosphopropanolamine (PPA, C3-bridge) or phosphobutanolamine (PBA, C4-bridge), but not PEA ligand (C2-bridge). Furthermore, we used well-documented, facile, and high-yield reaction schemes, exemplified in **Extended Data Fig. 6b**, to further extend the relevant structural space of phospholipid capping ligands. Besides the molecules with a single head group (**Extended Data Fig. 6c**), also molecules comprising several zwitterionic fragments (**Extended Data Fig. 6d**) were validated as efficient surfactants (**Supplementary Fig. 35**). The broad scope of NC core materials is seen in stable colloids obtained across the entire family of LHP NCs and for major kinds of lead-free materials - double perovskite NCs and low-dimensional Sb- and Bi-based metal halide NCs (**Extended Data Fig. 10**). Importantly, novel capping ligands can be applied not only through the post-synthetic ligand-exchange, but also in the direct synthesis of NCs (**Supplementary Note 7**). Future studies might extend to phospholipid-stabilized colloids oxides and fluorides, as well as two-dimensional inorganic materials such as MXenes or transition metal dichalcogenides.

References

1 Protesescu, L. *et al.* Nanocrystals of cesium lead halide perovskites (CsPbX$_3$, x = Cl, Br, and I): novel optoelectronic materials showing bright emission with wide color gamut. *Nano Lett.* **15**, 3692-3696, (2015).

2 Protesescu, L. *et al.* Monodisperse formamidinium lead bromide nanocrystals with bright and stable green photoluminescence. *J. Am. Chem. Soc.* **138**, 14202-14205, (2016).

3 Akkerman, Q. A., Raino, G., Kovalenko, M. V. & Manna, L. Genesis, challenges and opportunities for colloidal lead halide perovskite nanocrystals. *Nat. Mater.* **17**, 394-405, (2018).

4 Almeida, G., Infante, I. & Manna, L. Resurfacing halide perovskite nanocrystals. *Science* **364**, 833-

834, (2019).
5 Dey, A. *et al.* State of the art and prospects for halide perovskite nanocrystals. *ACS Nano* **15**, 10775-10981, (2021).
6 Boles, M. A., Ling, D., Hyeon, T. & Talapin, D. V. The surface science of nanocrystals. *Nat. Mater.* **15**, 141-153, (2016).
7 Owen, J. The coordination chemistry of nanocrystal surfaces. *Science* **347**, 615-616, (2015).
8 Tamarat, P. *et al.* The ground exciton state of formamidinium lead bromide perovskite nanocrystals is a singlet dark state. *Nat. Mater.* **18**, 717-724, (2019).
9 Park, Y. S., Guo, S. J., Makarov, N. S. & Klimov, V. I. Room temperature single-photon emission from individual perovskite quantum dots. *ACS Nano* **9**, 10386-10393, (2015).
10 Cherniukh, I. *et al.* Perovskite-type superlattices from lead halide perovskite nanocubes. *Nature* **593**, 535-542, (2021).
11 Kovalenko, M. V., Protesescu, L. & Bodnarchuk, M. I. Properties and potential optoelectronic applications of lead halide perovskite nanocrystals. *Science* **358**, 745-750, (2017).
12 Kwon, J. I. *et al.* Ultrahigh-resolution full-color perovskite nanocrystal patterning for ultrathin skin-attachable displays. *Sci. Adv.* **8**, eadd0697, (2022).
13 Kaplan, A. E. K. *et al.* Hong-Ou-Mandel interference in colloidal $CsPbBr_3$ perovskite nanocrystals. *Nat. Photonics* **17**, 775-780, (2023).
14 Luo, J. J. *et al.* Efficient and stable emission of warm-white light from lead-free halide double perovskites. *Nature* **563**, 541-545, (2018).
15 Lian, L. Y. *et al.* Efficient and reabsorption-free radioluminescence in $Cs_3Cu_2I_5$ nanocrystals with self-trapped excitons. *Adv. Sci.* **7**, 2000195, (2020).
16 Yakunin, S. *et al.* High-resolution remote thermometry and thermography using luminescent low-dimensional tin-halide perovskites. *Nat. Mater.* **18**, 846-852, (2019).
17 Schutt, K., Berry, J. J., Wheeler, L. M. & Rosales, B. A. Leveraging low-energy structural thermodynamics in halide perovskites. *ACS Energy Lett.*, 1705–1715, (2023).
18 Bodnarchuk, M. I. *et al.* Rationalizing and controlling the surface structure and electronic passivation of cesium lead halide nanocrystals. *ACS Energy Lett.* **4**, 63-74, (2019).
19 Imran, M. *et al.* Simultaneous cationic and anionic ligand exchange for colloidally stable $CsPbBr_3$ nanocrystals. *ACS Energy Lett.* **4**, 819-824, (2019).
20 Chen, Y. *et al.* Surface termination of $CsPbBr_3$ perovskite quantum dots determined by solid-state NMR spectroscopy. *J. Am. Chem. Soc.* **142**, 6117-6127, (2020).
21 Krieg, F. *et al.* Stable ultraconcentrated and ultradilute colloids of $CsPbX_3$ (X = Cl, Br) nanocrystals using natural lecithin as a capping ligand. *J. Am. Chem . Soc.* **141**, 19839-19849, (2019).
22 Krieg, F. *et al.* Colloidal $CsPbX_3$ (X = Cl, Br, I) nanocrystals 2.0: zwitterionic capping ligands for improved durability and stability. *ACS. Energy Lett.* **3**, 641-646, (2018).
23 Krieg, F. *et al.* Monodisperse long-chain sulfobetaine-capped $CsPbBr_3$ nanocrystals and their superfluorescent assemblies. *ACS Cent. Sci.* **7**, 135-144, (2021).
24 Liu, S. *et al.* Membrane-destabilizing ionizable phospholipids for organ-selective mRNA delivery and CRISPR-Cas gene editing. *Nat. Mater.* **20**, 701-710, (2021).
25 Zumbuehl, A. Artificial phospholipids and their vesicles. *Langmuir* **35**, 10223-10232, (2019).
26 Harayama, T. & Riezman, H. Understanding the diversity of membrane lipid composition. *Nat. Rev. Mol. Cell Bio.* **19**, 281-296, (2018).
27 Fedotenko, I. A., Holme, M. N., Tanasescu, R., Zaffalon, P. L. & Zumbuehl, A. Putting the 'P' into phospholipids. *Chimia* **65**, 859-862, (2011).
28 Magolda, R. L. & Johnson, P. R. A new efficient and versatile synthesis of alkyl prosphorylcholines. *Tetrahedron Lett.* **26**, 1167-1170, (1985).
29 Eibl, H. & Engel, J. Synthesis of hexadecylphosphocholine (miltefosine). *Prog. Exp. Tumor Res.* **34**, 1-5, (1992).
30 Fiore, M. The synthesis of mono-alkyl phosphates and their derivatives: an overview of their nature, preparation and use, including synthesis under plausible prebiotic conditions. *Org. Biomol. Chem.* **16**, 3068-3086, (2018).
31 Akkerman, Q. A. *et al.* Controlling the nucleation and growth kinetics of lead halide perovskite quantum dots. *Science* **377**, 1406-1412, (2022).
32 Swendsen, R. H. & Wang, J. S. Replica Monte Carlo simulation of spin glasses. *Phys. Rev. Lett.* **57**,

2607-2609, (1986).
33 Sugita, Y. & Okamoto, Y. Replica-exchange molecular dynamics method for protein folding. *Chem. Phys. Lett.* **314**, 141-151, (1999).
34 De Roo, J. *et al.* Highly dynamic ligand binding and light absorption coefficient of cesium lead bromide perovskite nanocrystals. *ACS Nano* **10**, 2071-2081, (2016).
35 Stelmakh, A., Aebli, M., Baumketner, A. & Kovalenko, M. V. On the mechanism of alkylammonium ligands binding to the surface of $CsPbBr_3$ nanocrystals. *Chem. Mater.* **33**, 5962-5973, (2021).
36 Yang, Y. *et al.* Entropic ligands for nanocrystals: from unexpected solution properties to outstanding processability. *Nano Lett.* **16**, 2133-2138, (2016).
37 Mir, W. J. *et al.* Lecithin capping ligands enable ultrastable perovskite-phase $CsPbI_3$ quantum dots for Rec. 2020 bright-red light-emitting diodes. *J. Am. Chem. Soc.* **144**, 13302-13310, (2022).
38 van Meer, G., Voelker, D. R. & Feigenson, G. W. Membrane lipids: where they are and how they behave. *Nat. Rev. Mol. Cell Bio.* **9**, 112-124, (2008).
39 Singh, R. P., Gangadharappa, H. V. & Mruthunjaya, K. Phospholipids: unique carriers for drug delivery systems. *J. Drug Deliv. Sci. Tec.* **39**, 166-179, (2017).
40 Zhang, Y. B., Sun, C. Z., Wang, C., Jankovic, K. E. & Dong, Y. Z. Lipids and Lipid Derivatives for RNA Delivery. *Chem. Rev.* **121**, 12181-12277, (2021).
41 Dorlo, T. P. C., Balasegaram, M., Beijnen, J. H. & de Vries, P. J. Miltefosine: a review of its pharmacology and therapeutic efficacy in the treatment of leishmaniasis. *J. Antimicrob. Chemoth.* **67**, 2576-2597, (2012).
42 Eibl, H. & Unger, C. Hexadecylphosphocholine - a new and selective antitumor drug. *Cancer. Treat. Rev.* **17**, 233-242, (1990).
43 Hahm, D. *et al.* Direct patterning of colloidal quantum dots with adaptable dual-ligand surface. *Nat. Nanotechnol.* **17**, 952-958, (2022).
44 Hahm, D. *et al.* Surface Engineered Colloidal Quantum Dots for Complete Green Process. *ACS Appl. Mater. Interfaces* **12**, 10563-10570, (2020).
45 Ye, X. C. *et al.* Structural diversity in binary superlattices self-assembled from polymer-grafted nanocrystals. *Nat. Commun.* **6**, 10052, (2015).
46 Cherniukh, I. *et al.* Shape-directed co-assembly of lead halide perovskite nanocubes with dielectric nanodisks into binary nanocrystal superlattices. *ACS Nano* **15**, 16488-16500, (2021).
47 Zhu, X. L. *et al.* Lead halide perovskites for photocatalytic organic synthesis. *Nat. Commun.* **10**, 2843, (2019).
48 Rosa-Pardo, I. *et al.* The synergy between the $CsPbBr_3$ nanoparticle surface and the organic ligand becomes manifest in a demanding carbon-carbon coupling reaction. *Chem. Commun.* **56**, 5026-5029, (2020).
49 Raino, G. *et al.* Ultra-narrow room-temperature emission from single $CsPbBr_3$ perovskite quantum dots. *Nat. Commun.* **13**, 2587, (2022).
50 Rainò, G. *et al.* Underestimated effect of a polymer matrix on the light emission of single $CsPbBr_3$ nanocrystals. *Nano Lett.* **19**, 3648-3653, (2019).

Acknowledgements
This work was financially supported by the Air Force Office of Scientific Research and the Office of Naval Research (award number FA8655-21-1-7013), by the Swiss National Science Foundation (National Centre of Competence in Research, NCCR Catalysis, Grant No.180544), by the European Research Council through the European Union's Horizon 2020 program (ERC Consolidator Grant SCALE-HALO, agreement no. 819740), as well as by the Swiss Innovation Agency (Innosuisse, Grant No. 32908.1 IP-EE)

Author contributions
V.M. and M.V.K. conceived the project. V.M. and M.S. synthesized phospholipids, and together with C.J.K. and J.A., tested them as capping ligands and evaluated ensemble optical properties. A.S. and A.B. conducted molecular dynamics simulations of NC-ligand interfaces, S.C.B. acquired and interpreted FTIR spectra; M.A. L.G.F., V.M. and A.S. acquired and analyzed REDOR spectra. N.S., S.B., and I.C. acquired high-resolution electron microscopy images; L.G.F. and G.R. conducted single-particle PL studies; Y.S. and D.N.D. performed photocatalytic studies; V.M., A.S. and M.V.K. wrote the manuscript with the contribution of all co-authors. M.V.K. supervised the work. All authors discussed the results and commented on the manuscript.

Competing financial interests: The authors declare no competing financial interest.

Materials & Correspondence Maksym V. Kovalenko (mvkovalenko@ethz.ch).

Correspondence and requests for materials should be addressed to M.V.K.

Data availability

The data that support the findings of this study are available on Zenodo public depository and from the corresponding author on reasonable request.

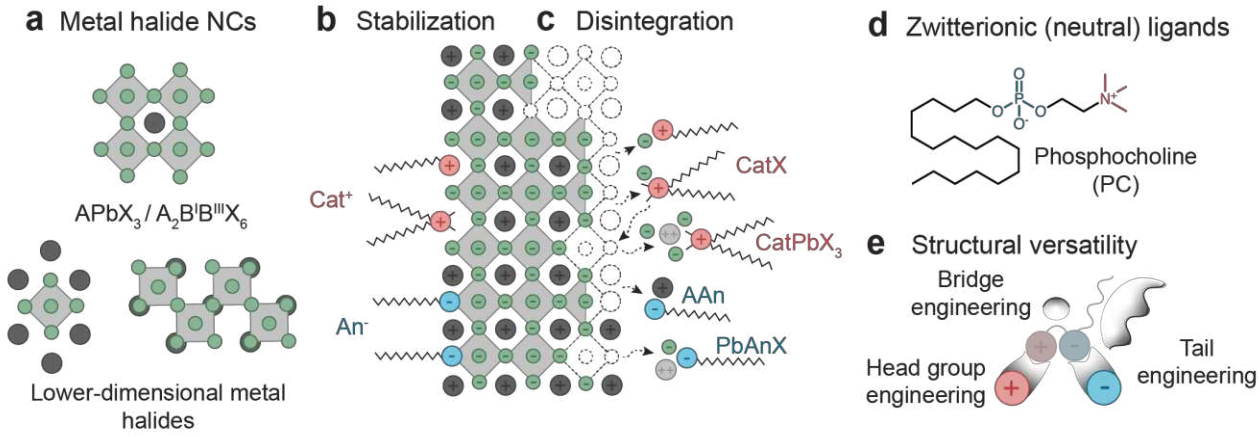

Fig. 1: Binding of zwitterionic ligands to surfaces of soft ionic metal halides.

a, Examples of ionic metal halides. **b,c,** Atomistic depiction of (**b**) surface stabilization and (**c**) disintegration of $APbX_3$ perovskite by common long-chain cationic (Cat^+) and anionic (An^-) ligands due to excess ligand quantity and low internal crystal energy. **d,e**, Zwitterionic molecules offer stronger (multidentate) binding and reduced reactivity owing to their neutral charge. Structural engineering of the head, bridge, and tail groups unlocks their broad utility for stabilizing diverse metal halide NCs and dispersing them in various media.

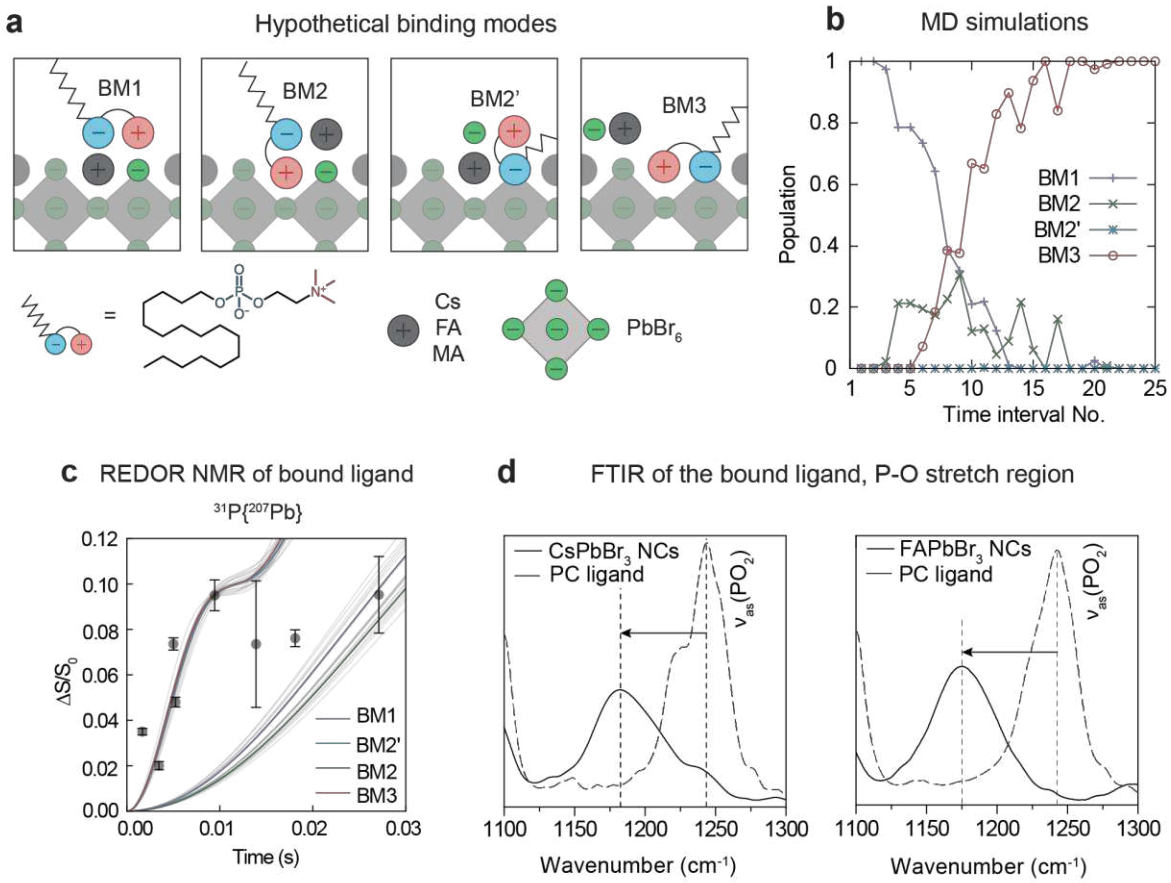

Fig. 2: Binding of zwitterionic ligands to the $FAPbBr_3$ NC surface

a, Schematics of different modes for binding of zwitterionic ligands, whose plausibility was assessed with replica-exchange MD simulations. **b**, Evolution of the binding mode populations, computed in a 50 ns-long replica-exchange MD simulation of a single PC ligand that was initially placed on the pristine FABr-rich (100) surface of $FAPbBr_3$. BM3 prevails in the ensemble in the late stages of the simulation. **c**, Results of a Rotational-Echo DOuble-Resonance (REDOR) NMR experiment for ^{31}P-^{207}Pb coupling supports the theoretical prediction that surface anchoring with the phosphate group. Theoretical REDOR curves were calculated using conformations obtained from the MD simulations. Dashed line represents initial slope fit of the experimental data. **d**, FTIR analysis of the (P-O) stretching region, wherein the P-O bond weakening upon ligand binding, *i.e.* P-O-Pb bridge formation, shifts the signal to lower frequencies.

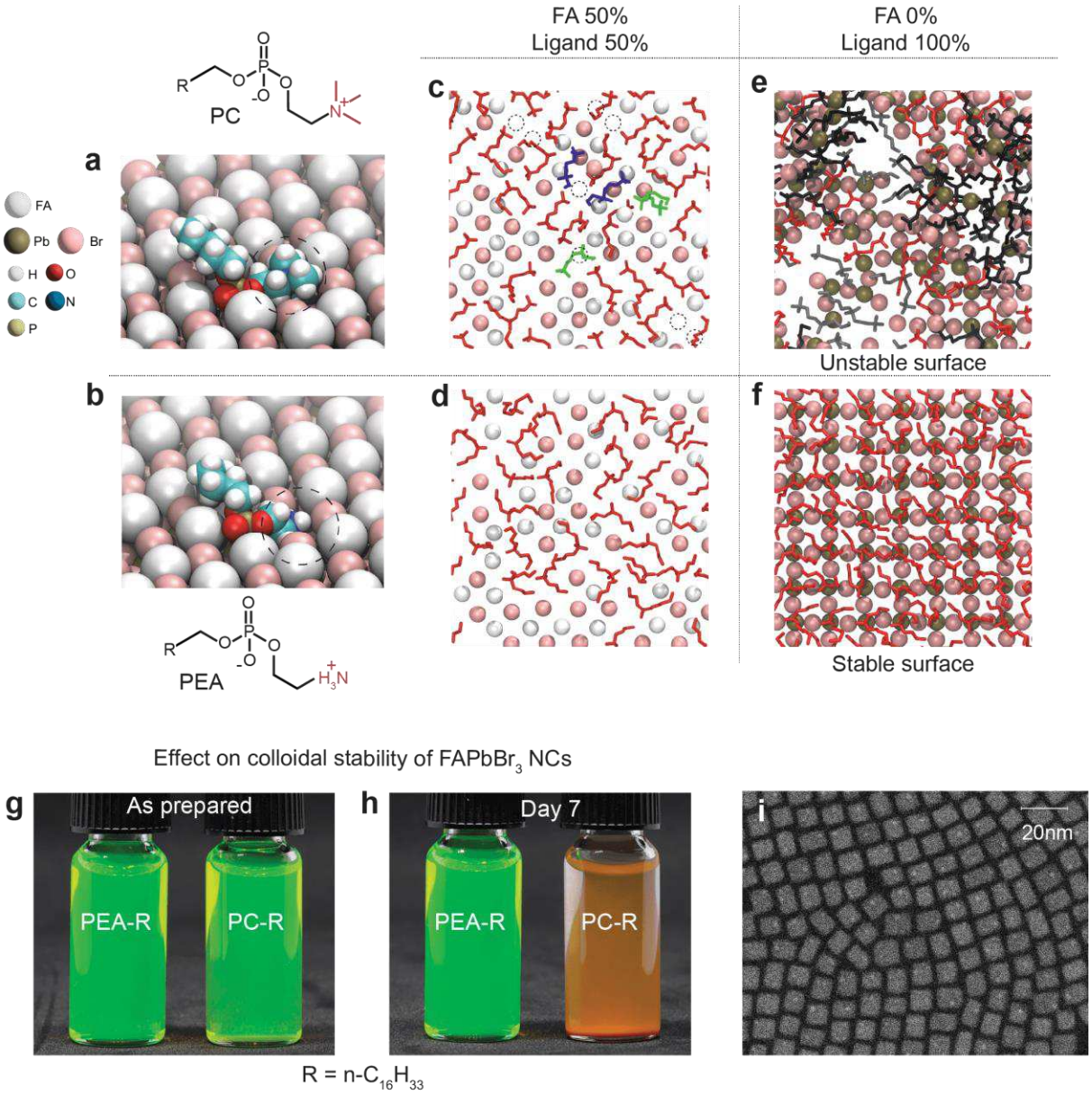

Fig. 3: Ligand head-group engineering

a,**b**, Geometries of the PC (**a**) and PEA (**b**) head groups on the (100) surface of $FAPbBr_3$, emphasizing the improved PEA fitness for the surface A-site. **c**-**f**, Snapshots from replica-exchange MD simulations of the $FAPbBr_3$ surfaces in which 50% (**c,d**) or 100% (**e,f**) of FABr pairs were substituted with the ligands. Ligand molecules are color-coded according to their binding mode – BM1 (blue), BM2 (green), BM2' (orange), and BM3 (red). Although stable surfaces are observed at 50% substitution with both ligands, a noticeable amount of PC ligands and FA and Br ions desorb from a PC-capped surface, leaving behind vacancies in the top-most surface layer (black dashed circles in **c**). At 100% substitution, the PC-capped surface starts to rupture (**e**), whereas it remains stable in the case of PEA ligand (**f**). **g,h,** Colloids of purified hexadecyl-PEA and -PC capped purified $FAPbBr_3$ NCs (8.5 nm): as prepared (**g**) and after seven days (**h**). **i**, Typical HAADF-STEM image of $FAPbBr_3$ NCs capped with the alkyl-PEA ligand.

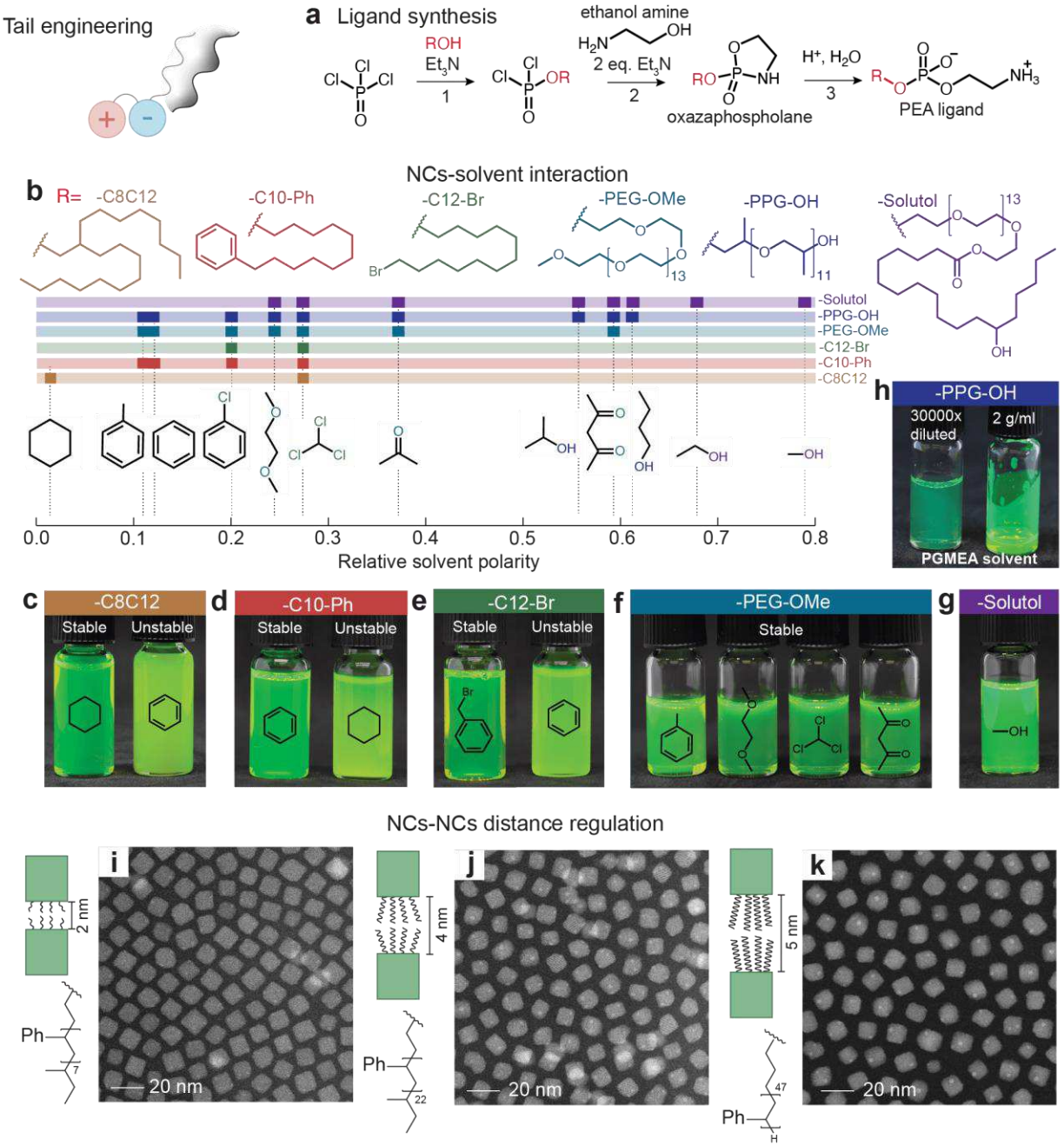

Fig. 4: Examples of functional tail engineering.

a, Synthesis scheme for PEA-ligands tested in this work, with 21 ligand tails shown in **Extended Data Fig. 6**. **b-g,** Different tails allow for matching the solvent polarity (**b**) with highly specific dispersibility, shown for $FAPbBr_3$ NCs (**c-e**) and $CsPbBr_3$ NCs (**f, g**). **h**, PPG-PEA-capped $CsPbBr_3$ NCs in PGMEA at a concentration of 2 g ($CsPbBr_3$) per mL of dispersion. **i-k**, Engineering inter-NC distance in monolayers of $CsPbBr_3$ NCs capped with PEA ligands with polystyrene tails by adjusting the ligand molecular weight: M_n=900 Da (**h**), 1200 Da (**i**) and 5000 Da (**j**).

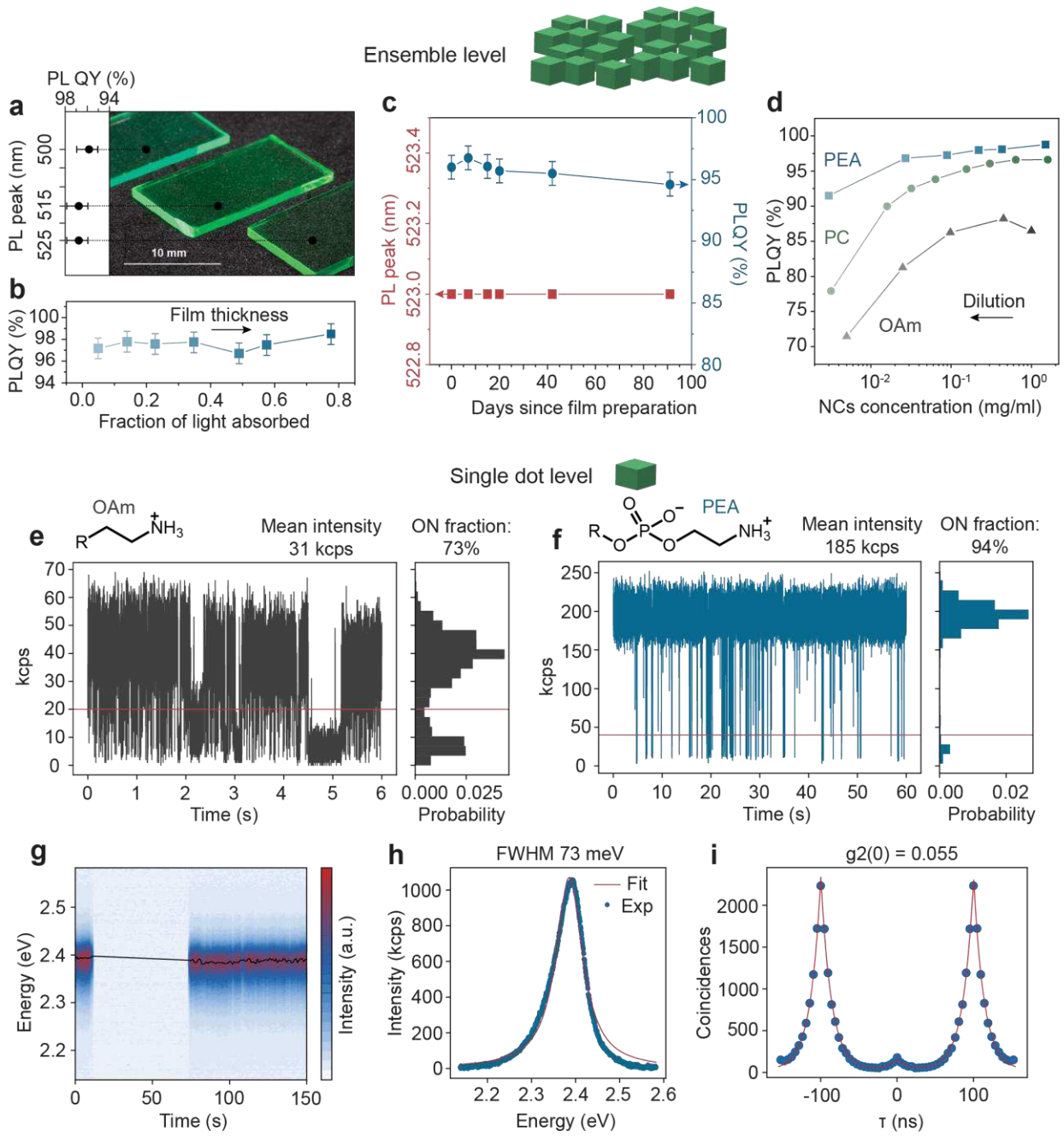

Fig. 5: Light emission from C8C12-PEA-capped $FAPbBr_3$ NCs on the ensemble and single dot levels.

a-d, Highlighted optical properties of $FAPbBr_3$ NCs in an ensemble. Films of $FAPbBr_3$ NCs of various sizes demonstrate equally high PLQY and tunable green emission (**a**). High PLQY is retained in thick films (**b**) and is not influenced by film storage in ambient conditions for at least 90 days (**c**). PLQY of >90% is preserved upon ≈1'000-fold dilution of C8C12-PEA capped NCs with octane, whereas a pronounced drop is observed for C8C12-PC and OAm capped NCs (**d**), indicative of dilution-induced surface degradation. **e-i,** Optical properties of $FAPbBr_3$ NCs at the single particle level. Single PEA-capped NCs exhibit high brightness and suppressed PL blinking (**e,f**), good PL stability (**g**), narrow PL linewidth (FWHM) (**h**) and high single-photon purity (**i**). PLQY measurement error in **d** is ±1%.

Methods

Computational model

The surface of perovskite NCs modeled using a crystal slab terminated with (100) crystallographic planes, in line with the HR-STEM images of $FAPbBr_3$ and $CsPbBr_3$ NCs capped with alkylphospholipid ligands (**Supplementary Fig. 5**). Both ABr- and PbBr-rich lattice terminations was considered. One of the slab surfaces was then passivated by placing a certain number of ligands (1, 32 or 64) at a distance of 0.5 nm from the surface (measured to the head group). The ligand tail was truncated at five carbon atoms to reduce computational cost. If needed, some ion pairs were removed from the surface to yield the desired system stoichiometry defined by two quantities – ligand concentration $[Lig] = \frac{N_{lig}}{64}$, and ABr concentration $[ABr] = \frac{N_{ABr}}{64}$. Finally, the system was solvated with toluene. Further details of the slab model can be found in **Supplementary Note 1.** Interactions between ions comprising the slab were modeled by Coulomb and Lennard-Jones potentials, with parameters adopted from Ref. [54-56]. This classical perovskite model was tested in simulations of bulk $CsPbBr_3$ and $FAPbBr_3$ crystals with a fully anisotropic pressure coupling and yielded good agreement with experimental structural properties (**Supplementary Fig. 6**). OPLS-AA force field[57-59] was used to model interactions between atoms in the organic part of the system. Ligand parameters were taken from the corresponding models of phospholipids[60,61]. Missing O-C-C-C and O-C-C-H dihedral parameters at the point of attachment of the tail to the head group were taken from the analogous dihedral parameters for ether/alcohol[62].

Replica-exchange MD simulations

The complete simulation boxes were equilibrated for 20 ps in the NVT ensemble with positions of all ions and ligand head groups tightly restrained and then for 1+10 ns in the NPT ensemble with released restraints. In all simulations, positions of lead ions in the middle layer of the slab were restrained to the origin of the z-axis and to their crystallographic positions in x and y directions by applying weak harmonic restraining potential with a force constant of k = 1000 kJ/(mol·nm^2), to prevent floating of the slab across the simulation box.

The final pre-equilibrated structures were used as starting points for replica-exchange MD simulations[33] in the NVT ensemble. 120 replicas were exponentially distributed between 300 and 2200 K, allowing the efficient crossing of potential energy barriers. Exchanges between neighboring replicas were attempted every one ps,

and each replica was simulated for 50 ns. The average exchange rate was ensured to be above 10% for all neighboring replica pairs. Setting all atomic masses to 12 a.u. allowed us to increase the simulation time-step to 1 fs without affecting the configurational phase space of the system. Special restraining potentials were employed to prevent the crystal's high-temperature melting and limit diffusive movements of the ions and ligand molecules. These are discussed in more detail in **Supplementary Note 2.**

All reported simulations were performed using GROMACS software package[63]. Electrostatic interactions were computed using the smooth particle-mesh Ewald method[64].

Binding mode populations were computed in two steps. First, distances from the ligands' nitrogen and phosphorus atoms to the middle atomic plane of the slab, d_{N-slab} and d_{P-slab}, were calculated over the whole replica-exchange MD run and plotted as a 2D map. At most, four well-defined clusters were observed in the case of AX-terminated surfaces, which were assigned to four different binding modes – BM1, BM2, BM2' and BM3 (**Extended Data Fig. 1**). The broad tail which extends to long ligand-slab separations was attributed to unbound ligands. In the next step, ligands were classified according to their binding mode using the corresponding cut-offs on the *N-slab* and *P-slab* distances. Binding mode populations were computed as ensemble averages within 2-ns intervals and presented as time traces.

PEA, PPA, and PBA ligands synthesis

The synthesis route starting with alcoholysis of phosphorous oxychloride was adopted from Ref.29. Solution of alcohol substrate (0.025 mol; 1 eq.) dissolved in dry THF (25 ml) along with triethylamine (0.275 mol; 1.1 eq.; 3.83 ml) is added dropwise with vigorous stirring to a solution of phosphorous oxychloride (0.03 mol; 1.2 eq.; 2.78 ml) in THF (2.5 ml) on an ice water bath. The reaction mixture is subsequently kept at 20 °C for 15 minutes to complete the reaction. Next, ethanolamine (0.03 mol; 1.2 eq.; 1.81 ml) and triethylamine (0.06 mol; 2.4 eq.) in THF (37.5 ml) are added dropwise under vigorous stirring to the reaction mixture kept in a room-temperature water bath. Subsequently, the mixture is heated to 40 °C for 15 min to complete the ring closure. Finally, the reaction mixture is filtered to remove precipitated triethylamine hydrochloride, and the filtrate solution is dried. An oily residue, *i.e.,* alkyl-2-oxo-1,2,3-oxazaphospholane, is dissolved in a mixture of acetic acid (5.7 ml) and distilled water (2.6 ml) at 70 °C. After 30 min, ring scission at the P-N bond is complete, and the product is separated by beating with acetone (125-150 ml). After cooling to 10 °C,

alkylphosphoethanolamine is collected and dried overnight under a vacuum at 40-50 °C. 3-aminopropan-1-ol and 4-aminobutanol-1-ol were used instead of 2-aminoethan-1-ol for PPA or PBA ligands. For PBA, the hydrolysis step was conducted at 90 °C.

PC ligands synthesis

Synthesis procedure beginning with the alcoholysis of 2-chloro-2-oxo-1,3,2-dioxaphospholane (COP) was adopted from Ref.[65]. A solution of COP (0.7 mol; 1eq.; 10g) in dry THF (30 ml) was added dropwise to a mixture of alcohol substrate (0.7 mol; 1 eq.) and triethylamine (0.7 mol; 1 eq.) in dry THF (140 ml) at 0 °C under vigorous stirring. After the addition, stirring was continued for one h at room temperature. After filtering, the filtrate solution was concentrated by at least a factor of two or by evaporation and dry acetonitrile (150 ml) was added, and the reaction mixture was placed into a glass pressure bottle. At -20 °C, 2M trimethylamine in THF (0.14 mol; 2 eq.; 70 ml) was added and the reaction was carried at 70 °C for 12 h. After 12 h, the reaction mixture was cooled to -20 °C to precipitate the product. The product was then filtered off and dried under a vacuum overnight.

Further synthetic conditions and characterization of all obtained ligands can be found in **Supplementary Figs. 13-14** and **Supplementary Note 4.**

'Ligand-exchange' synthesis of $CsPbBr_3$, $FAPbBr_3$, and $MAPbBr_3$ NCs capped with zwitterionic ligands. NCs were synthesized according to the modified TOPO-DOPA procedure described elsewhere[31]. Pb precursor was prepared from $PbBr_2$ (0.2 mmol, 73.4 mg) and TOPO (90%) (1.1 mmol, 429.6 mg) dissolved in n-octane (2.5 ml) at 120 °C on a hotplate in the air. Pb precursor is then diluted with various quantities of hexane to obtain NC of different sizes. Cs precursor was obtained by reacting Cs_2CO_3 (100 mg) with DOPA (1 mL) in octane (2 mL) at 120 ºC, followed by dilution with hexane (27 mL). FA precursor was prepared from formamidine acetate, 64 mg (0.61 mmol), DOPA (3ml), and OA (2ml), dissolved in n-octane (5 ml) at 120 °C in a 40 ml vial on a hot plate in the air. MA precursor was prepared by mixing MA in THF (2M, 0.3 ml) along with DOPA (3 ml), OA (2 ml), and n-octane (5 ml). To synthesize NCs, A precursor is swiftly injected into the Pb precursor upon stirring at RT and left for a defined amount of time to nucleate and grow NCs, followed by the addition of the zwitterionic ligands. Synthesis details, specific to NC sizes and compositions, and further

characterization can be found in the **Supplementary Note 5**, **Supplementary Tables 4-10, Supplementary Figs. 15-17**.

Purification of zwitterion-capped NCs

When NCs remain dispersed in n-hexane after the ligand exchange, 2-3 equivalents of an anti-solvent (list of anti-solvents is given in **Supplementary Table 11**) are added to precipitate NCs, followed by centrifugation. The colorless supernatant is discarded, and the precipitate is redispersed in a desired solvent. When the ligand-capped NCs are incompatible with hexane (*e.g.,* polystyrene, polyethyglycol-based ligands), they precipitate after ligand exchange. NCs are further collected by centrifugation and redispersed in suited solvent, completing the first washing cycle. Further, 3-4 equivalents of n-hexane (or other suitable anti-solvent) are added to precipitate NCs again for the next washing cycle. The washing cycle can be repeated as many times as required. After three cycles, impurities of TOPO, DOPA, and OA are absent, as evidenced by ^{31}P NMR (**Supplementary Fig. 25**). Further details can be found in **Supplementary Note 6** and **Supplementary Fig. 25-26**.

Ligand coverage estimation by ^{31}P NMR

To estimate the ligand coverage, stable and purified NCs colloids in toluene capped with PEA or PC ligands were dissolved in DMSO-d6, destroying NCs and freeing the bound ligands. A known amount of phosphor-containing standard (*e.g.,* tetrabutylphosphonium bromide) was added to the toluene-DMSO-d6 sample, and the ^{31}P NMR 1D spectrum was measured. Integration of the P signal was readily recalculated to the ligand concentration. NCs concentration was estimated from extinction coefficient[34], and absorption was measured from the sample before destruction with DMSO.

FTIR spectroscopy

Ligand binding mode in PEA- and PC-capped perovskite NCs was assessed with FTIR spectroscopy in conjunction with ab-initio molecular dynamics (AIMD) simulations (Details in **Supplementary Note 3**). FTIR spectra of solid-state samples, *i.e.,* ligands and dry NC powders, were obtained in a N_2-filled glovebox via a ThermoFisher Nicolet iS5 FTIR spectrometer with a deuterated triglycine sulfate (DTGS) detector, a KBr beam splitter, and an iD5 attenuated total reflectance (ATR) unit comprising a diamond crystal.

Solid-state NMR spectroscopy

^{31}P-^{207}Pb REDOR experiments were performed on a Bruker narrow-bore 16.4 T (600 MHz) and 9.4 (400 MHz) TNMR spectrometers equipped with a Bruker Avance III HD console. All experiments were performed on a 2.5 mm HXY probe configured in a ^{1}H-^{31}P-^{207}Pb mode. A MAS frequency of 20 kHz was used for all experiments. The ^{1}H π/2-pulse was optimized to 3 µs, for ^{31}P to 6.1 µs and ^{207}Pb to 6.5 µs. Chemical shifts were externally referenced to tetramethylsilane (^{1}H), phosphoric acid (^{31}P), and tetramethyl lead (^{207}Pb). ^{31}P spectra were acquired with a π-pulse excitation and ^{1}H decoupling (SPINAL64) during acquisition. A recycle delay of 1 second was used. ^{207}Pb spectra were acquired using a π/2 - π Hahnecho sequence. The echo delay was set to 1 rotor cycle (50 µs). A recycle delay of 0.5 s was used.

^{1}H-^{31}P(^{207}Pb) cpREDOR experiments were performed on a Bruker wide-bore 14.1 T NMR spectrometer equipped with a Bruker Avance III HD console. All experiments were performed on a 3.2 mm HXY DNP probe configured in a ^{1}H-^{31}P-^{207}Pb mode. A MAS frequency of 9 and 11 kHz was used for all experiments. The ^{1}H π/2-pulse was optimized to 2.7 µs. The ^{31}P π/2-pulse was optimized to 7 µs. A saturation pulse train with 16 π/2-pulses on ^{1}H and ^{31}P was applied. A ramp pulse (2 ms) was used for ^{1}H-^{31}P contact. ^{1}H-^{31}P cp spectra with varying recoupling times were acquired with (S) and without (S_0) dephasing pulses on ^{207}Pb. The duration of dipolar recoupling was incremented linearly. Dephasing was induced by ^{207}Pb π-pulses (15.2 µs). A recycle delay of 3 seconds was used. The recoupling curves were obtained by plotting (S_0-S)/S_0 versus the recoupling time.

The recoupling curves $\tilde{S}(N_{rot})$ are determined as

$$\tilde{S}(N_{rot}) = 1 - \frac{S(N_{rot})}{S_0(N_{rot})}$$

Where $S(N_{rot})$ and $S_0(N_{rot})$ are the integrals of the NMR spectra with and without dephasing pulses at varying recoupling times (expressed as number of rotations N_{rot}). Using uncertainty propagation, the corresponding error $\sigma_{\tilde{s}}(N_{rot})$ is

$$\sigma_{\tilde{s}}(N_{rot}) = \sqrt{\left(\frac{\partial}{\partial S(N_{rot})}\,\tilde{S}(N_{rot})\right)^2 \sigma_S^2(N_{rot}) + \left(\frac{\partial}{\partial S_0(N_{rot})}\,\tilde{S}(N_{rot})\right)^2 \sigma_{S_0}^2(N_{rot})}$$

$$= \sqrt{\frac{\sigma_S^2(N_{rot})}{S_0^2(N_{rot})} + \frac{\sigma_{S_0}^2(N_{rot})\, S^2(N_{rot})}{S_0^4(N_{rot})}}$$

The errors $\sigma_S(N_{rot})$ and $\sigma_{S_0}(N_{rot})$ are determined from the noise level of the spectrum and are identical as number of scans and noise levels are identical.

Computation of theoretical REDOR curves

Theoretical REDOR curves (BM1-BM3) were generated by our Python implementation of an approach reported elsewhere[20]. The source code is available at https://gitlab.ethz.ch/kovalenkolab/redor. This approach simulates REDOR curves for a multi-spin system (> two spins), including heteronuclear coupling, while assuming that homonuclear coupling can be neglected. This assumption holds for the initial slope of the REDOR curve (short dephasing times).[66] The geometries for the theoretical curves were either based on the crystal structure of $FAPbBr_3$ or chosen from the replica-exchange MD simulation of a single PC ligand on the FABr-terminated perovskite surface. Ten randomly selected structures were used for each binding mode in the latter case. Since BM2' was not observed in this simulation, a separate 10 ns plain MD simulation with the ligand initially placed in BM2' was performed. We note that BM2' was found to be metastable across the entire simulation. The theoretical REDOR curve on Fig. 2c was scaled by coefficient 0.3 to fit the initial data slope to account for dynamics and inefficient recoupling due to the potential broadening of ^{207}Pb signal of Pb atoms bound to phosphate.

Electron microscopy

TEM images were collected using a Hitachi HT7700 microscope operated at 100 kV. HAADF-STEM images were obtained using an FEI Titan Themis aberration-corrected microscope operated at 300 kV and with a probe-corrected cubed Thermo Fisher Scientific Themis Z Microscope operating at 300 kV with a probe semi-convergence angle of 20 rad. Images were processed using Image J.

Optical spectroscopy

Room-temperature photoluminescence (PL) spectra of purified QDs were recorded with a Fluorolog iHR 320 Horiba Jobin Yvon with an excitation at 350 nm. Absorption spectra were recorded with a Jasco V670 spectrometer. PL quantum yield (PLQY) was measured using the Quantaurus-QY spectrometer C11347-11

from Hamamatsu Photonics; for samples with absorbance higher than 0.4, a self-absorption correction procedure was used as implemented in the software (U6039-05 for Quantaurus QY). Single-dot spectroscopy and related sample preparation were conducted under a nitrogen atmosphere. Firstly, the NC solutions were diluted by a factor of 30 000 – 60 000 with dry and filtered n-octane (99+% extra dry, *Acros Organics*). A sparse NC film was obtained by spin-coating 100 µL of the diluted solution at 150 reps for 60 seconds onto a clean cover glass (thickness 170 ± 5 µm; diameter 25 mm; *Thorlabs*). Micro-PL measurements were carried out with a home-build setup under irradiation with a pulsed 405 nm laser (10 MHz, < 50 ps pulses, < 100 W/cm^2, *Picoquant*). The laser is focused (1/e^2 = one µm) by an oil immersion objective (NA = 1.3) onto the sample, and the same objective collects the emitted light. The collected light is passed through a dichroic mirror to filter out the residual light from the excitation laser and sent either to a Hanbury-Brown and Twiss (HBT) experiment or to a monochromator and EMCCD camera (1s-binning, *Princeton Instruments*). The HBT experiment consists of a 50/50 beam splitter, two avalanche photodiodes (temporal resolution = 250 ps, *Excelitas*), and photon-counting electronics (*Picoquant*), enabling the acquisition of time-tagged time-resolved (TTTR) fluorescence data. Single-dot measurements were carried out in the weak excitation regime at a fluence of 0.8 to 1.3 µJ/cm^2 (<1 exciton per pulse). The spectra of the NCs were obtained by averaging the first five frames of the spectra series and fitted with a Lorentzian peak to find the peak centre and FWHM. The second-order correlation function ($g^2(\tau)$) was calculated from the TTTR data with the *pycorrelate* package employing the algorithm by Laurence et al.[67] and fitted by a biexponential function (shared lifetimes, no constant offset) to predict the $g^2(0)$. The blinking traces were obtained by binning the TTTR data into 1 ms bins, and the fraction of time spent in the ON state was determined by thresholding after visual inspection of intensity histograms and traces (**Supplementary Fig. 30**).

Photocatalysis with $CsPbBr_3$ NCs

Benzyl bromide (69.5 µl) and a photocatalyst ($CsPbBr_3$ NCs, 1.35 mg) were combined with the solvent of choice (1 mL) and N,N-diisopropylethylamine (DIPEA, 306 µl) in a 4-mL vial that is then sealed with Parafilm. The vial is placed in the temperature controlled photoredox device PhotoRedOx TC from HepatoChem (HCK1006-01-025) equipped with 450 nm blue LED (30 W, 250 V) for 4 hours at 30 °C. After this time, the

reaction mixture was transferred to a round bottom flask with the help of dichloromethane and all solvent was evaporated. The dry leftover was dissolved in 0.5-0.6 ml of $CDCl_3$ for NMR (300 Hz) to analyse the product yield.

Additional references

51 Chen, O. *et al.* Compact high-quality CdSe-CdS core-shell nanocrystals with narrow emission linewidths and suppressed blinking. *Nat. Mater.* **12**, 445-451, (2013).

52 Shi, J. J. *et al.* All-optical fluorescence blinking control in quantum dots with ultrafast mid-infrared pulses. *Nat. Nanotechnol.* **16**, 1355-1361, (2021).

53 Chen, Y. *et al.* "Giant" multishell CdSe nanocrystal quantum dots with suppressed blinking. *J. Am. Chem. Soc.* **130**, 5026-5027, (2008).

54 de Araujo, A. S., Sonoda, M. T., Piro, O. E. & Castellano, E. E. Development of new Cd^{2+} and Pb^{2+} Lennard-Jones parameters for liquid simulations. *J. Phys. Chem. B* **111**, 2219-2224, (2007).

55 Lybrand, T. P., Ghosh, I. & Mccammon, J. A. Hydration of chloride and bromide anions - determination of relative free-energy by computer-simulation. *J. Am. Chem. Soc.* **107**, 7793-7794, (1985).

56 Aqvist, J. Ion water interaction potentials derived from free-energy perturbation simulations. *J. Phys. Chem.* **94**, 8021-8024, (1990).

57 Jorgensen, W. L. & Tirado-Rives, J. Potential energy functions for atomic-level simulations of water and organic and biomolecular systems. *Proc. Natl. Acad. Sci. U.S.A.* **102**, 6665-6670, (2005).

58 Dodda, L. S., Vilseck, J. Z., Tirado-Rives, J. & Jorgensen, W. L. 1.14*CM1A-LBCC: localized bond-charge corrected cm1a charges for condensed-phase simulations. *J. Phys. Chem. B* **121**, 3864-3870, (2017).

59 Dodda, L. S., Cabeza de Vaca, I., Tirado-Rives, J. & Jorgensen, W. L. LigParGen web server: an automatic OPLS-AA parameter generator for organic ligands. *Nucleic Acids Res.* **45**, 331-336, (2017).

60 Maciejewski, A., Pasenkiewicz-Gierula, M., Cramariuc, O., Vattulainen, I. & Rog, T. Refined OPLS all-atom force field for saturated phosphatidylcholine bilayers at full hydration. *J. Phys. Chem. B* **118**, 4571-4581, (2014).

61 Kulig, W., Pasenkiewicz-Gierula, M. & Rog, T. Cis and trans unsaturated phosphatidylcholine bilayers: a molecular dynamics simulation study. *Chem. Phys. Lipids* **195**, 12-20, (2016).

62 Jorgensen, W. L., Maxwell, D. S. & Tirado-Rives, J. development and testing of the OPLS all-atom force field on conformational energetics and properties of organic liquids. *J. Am. Chem. Soc.* **118**, 11225-11236, (1996).

63 Van Der Spoel, D. *et al.* GROMACS: fast, flexible, and free. *J. Comput. Chem.* **26**, 1701-1718, (2005).

64 Essmann, U. *et al.* a smooth particle mesh Ewald method. *J. Chem. Phys.* **103**, 8577-8593, (1995).

65 Kang, E. C., Kataoka, S. & Kato, K. Synthesis and properties of alkyl phosphorylcholine amphiphiles with a linear and an asymmetrically branched alkyl chain. *B. Chem. Soc. Jpn.* **78**, 1558-1564, (2005).

66 Goetz, J. M. & Schaefer, J. REDOR dephasing by multiple spins in the presence of molecular motion. *J. Magn. Reson.* **127**, 147-154, (1997).

67 Laurence, T. A., Fore, S. & Huser, T. Fast, flexible algorithm for calculating photon correlations. *Opt. Lett.* **31**, 829-831, (2006).

Extended data figures

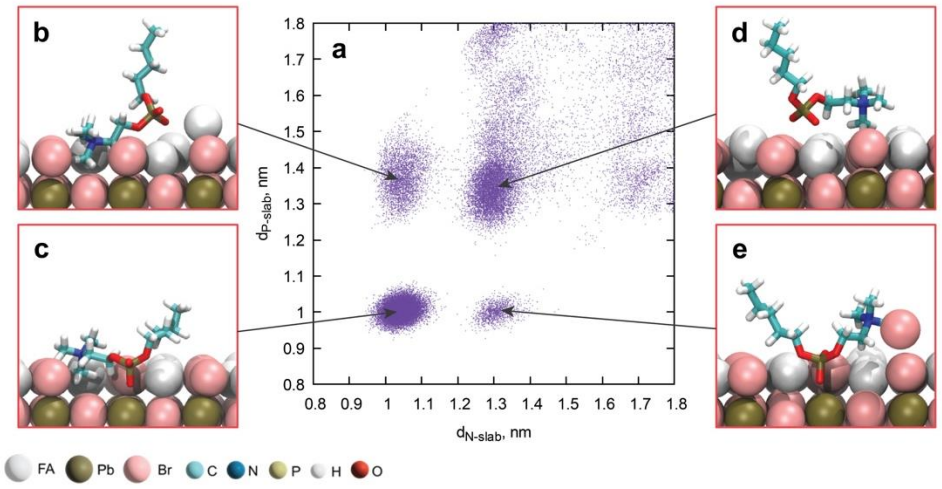

Extended Data Fig. 1: Classification of ligand binding modes

a, A typical map of configurations observed in replica-exchange MD simulations of the PC ligand on the (100) $FAPbBr_3$ surface. $d_{N\text{-}slab}$ and $d_{P\text{-}slab}$ define distances from the ligand head groups (nitrogen and phosphorus atoms, correspondingly) to the middle atomic plane of the slab. Four well-defined clusters of configurations correspond to the different binding modes of the ligand (**Fig. 2**). The diffuse region at large ligand-slab separations corresponds to free ligands. **b-e,** Snapshots of the observed binding modes - BM2 (**b**), BM3 (**c**), BM1 (**d**) and BM2'(**e**).

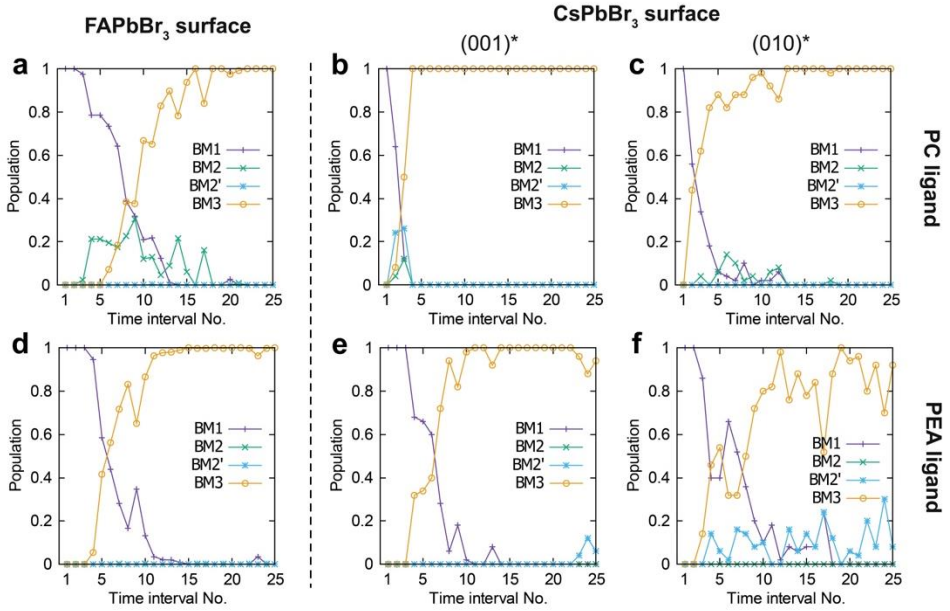

Extended Data Fig. 2: Generality of the prediction that zwitterionic ligands tend to displace both A and X ions from the perovskite surfaces

a-f, Evolution of binding mode populations in replica-exchange MD simulations of single PC (**a,b,c**) and PEA (**d,e,f**) ligand molecules on the $FAPbBr_3$ surface (**a,d**), (001) $CsPbBr_3$ surface (**b,e**), and (010) $CsPbBr_3$ surface (**c,f**). Binding with a displacement of both A and X ions (BM3) is thermodynamically preferred in all studied systems. *Crystallographic orientations refer to the primitive unit cell of $CsPbBr_3$ (see **Supplementary Note 1** for more details).

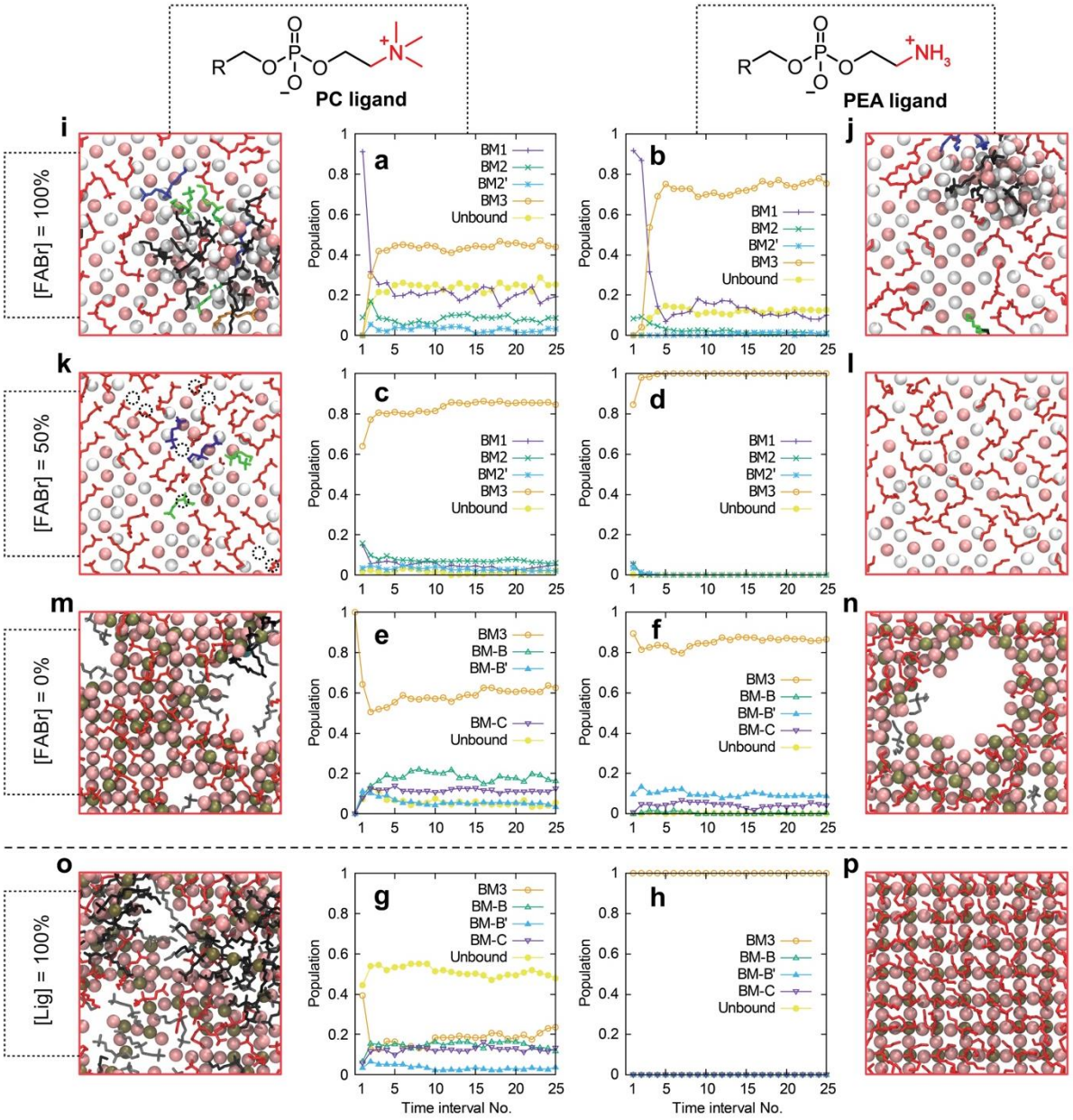

Extended Data Fig. 3: $FAPbBr_3$ surfaces at various [FABr] and [Lig] concentrations

a-f, Evolution of binding mode populations in systems with [Lig] = 50% and with a varying amount of surface FABr – 100% (**a,b**), 50% (**c,d**), and 0% (**e,f**). **g,h,** Evolution of binding mode populations in systems with [Lig] = 100% and [FABr] = 0%. In all scenarios, BM3 was identified as a dominant binding mode. The population of BM3 is also systematically higher for PEA ligand compared to PC, indicating a better fit of the former to the $FAPbBr_3$ surface. In addition, some new binding modes were discovered in systems where the rupture of the PbBr underlayer is observed – BM-B (ammonium in the PbBr layer), BM-B' (phosphate in the PbBr layer), and BM-C (both ammonium and phosphate in the PbBr layer). However, these are marginal and are encountered only along the phase boundaries between the newly exposed FABr- and the original PbBr-terminated surfaces. **i-p**, Corresponding MD snapshots with ligands being color-coded according to their binding mode – BM1 (blue), BM2 (green), BM2' (orange), BM3 (red), unbound (black), and other (gray).

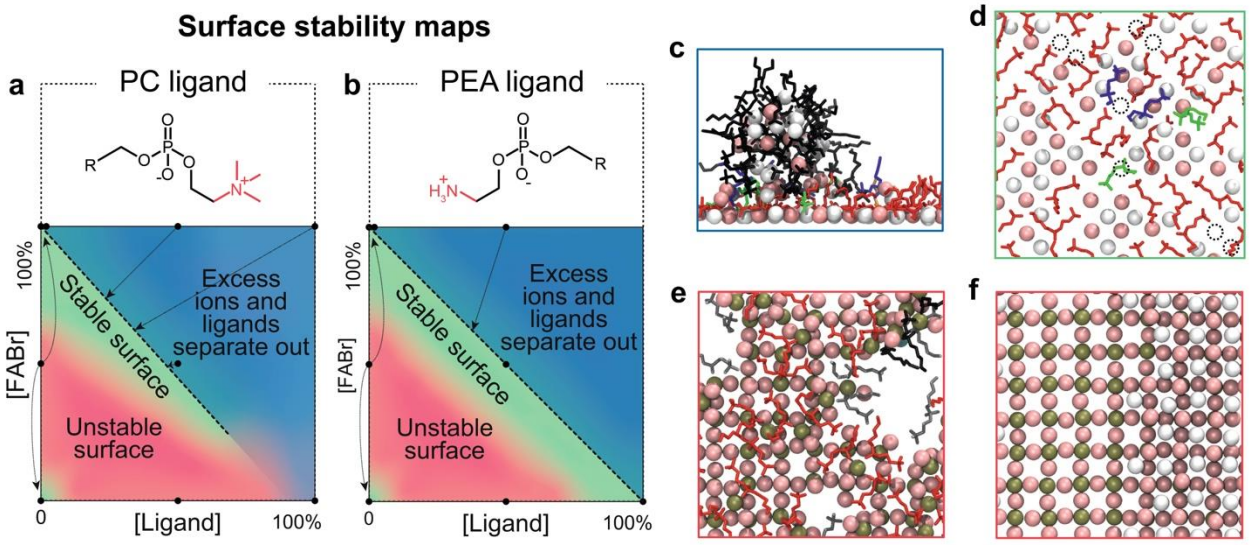

Extended Data Fig. 4: Stoichiometry-dependent stability of (100) $FAPbBr_3$ surfaces
a,b, Surface stability maps as a function of ligand and FABr concentrations computed for PC (**a**), and PEA (**b**) ligands. **c-f**, MD snapshots that illustrate three different regions observed on the stability maps. At high ligand+FABr concentrations, excess ions and ligands separate from the surface (blue area on the map) (**c**). As a result, the system acquires equilibrium stoichiometry corresponding to the green region on the map (**d**). At low ligand and/or FABr concentrations the surface becomes unstable again (a red region on the map) – segregation into two surfaces is observed for incomplete FABr passivation (**f**), whereas partial coverage solely with the ligand causes rupture of the PbBr underlayer (**e**). Ligand molecules in the snapshots are color-coded according to their binding mode – BM1 (blue), BM2 (green), BM2' (orange), BM3 (red), unbound (black), and other (gray).

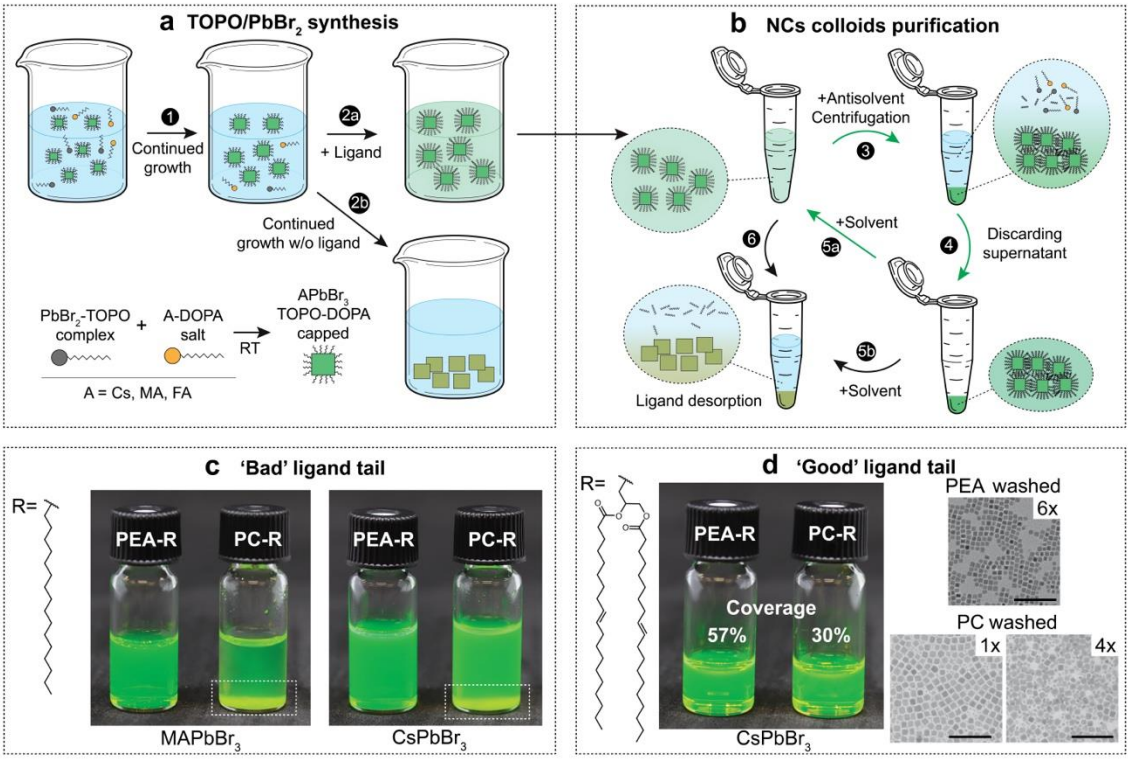

Extended Data Fig. 5: Synthesis of $APbBr_3$ NCs and testing of ligands

a, In TOPO-DOPA synthesis,[31] $PbBr_2$-trioctylphosphine (TOPO) complex reacts with diisooctylphosphinic acid (DOPA) salt of the corresponding A cation at room temperature, yielding monodisperse NCs (**1**). TOPO and DOPA are known as "bad ligands" and can be readily exchanged for zwitterion ligands (**2a**). If no capping ligands are added promptly after NCs are formed, the NCs rapidly lose their colloidal and structural integrity (**2b**). **b,** To purify phospholipid-capped NCs (see also **Supplementary Note 6**), a suited antisolvent is added, followed by centrifugation (**3**), whereas a supernatant containing unreacted precursors and free ligand molecules is discarded (**4**). If the ligand is' good', the resulting NCs pellet is redispersed in a suited solvent, yielding a stable colloid (5a). With a 'bad' ligand, NCs redisperse incompletely, do not redisperse (**5b**), or lose their colloidal integrity upon storage (**6**). Such a purification cycle (steps **3**, **4**, and **5a**) can be repeated several times. **c,d,** In this experiment, two head groups and two tails were compared. Combining a 'bad' head group and a 'bad' tail (**c**) leads to the worst colloidal stability, while combining a 'bad' head group and a 'good' tail might still yield long-term stable colloids (**d**). Similar to $FAPbBr_3$, $MAPbBr_3$, and $CsPbBr_3$ (**c**) NCs with PC head-group and a 'bad' hexadecyl tail precipitate after three rounds of purification, with visible deposit highlighted with a white box on the photo. $CsPbBr_3$ NC colloids with both PEA or PC head-groups and a 'good' glycerodioleyl tail (**d**, commercially available) yield stable colloids; however, with different ligand coverage, in agreement with MD prediction. Furthermore, PC-based surface ligation is more labile, with both "good" and "bad" tails: NCs tend to increase their mean particle size (inset TEM images, scale bars 50 nm) and acquire more irregular NC morphology with storage or several purification cycles.

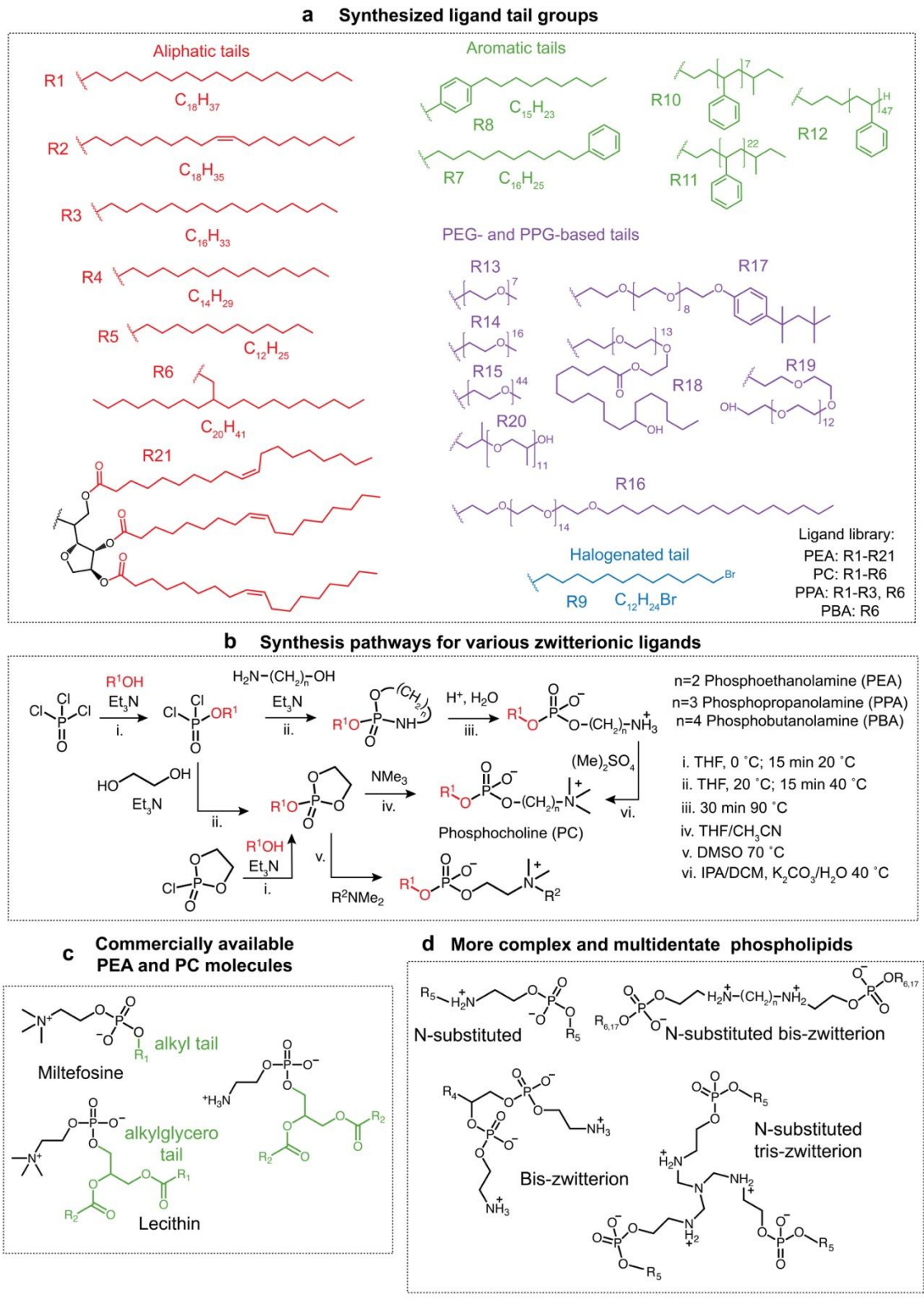

Extended Data Fig. 6: Survey of synthesized and commercial phospholipid ligands
a, Tail groups of the synthesized PEA ligand library. **b,** Synthetic pathways for PPA, PEA, PC and N-alkyl substituted PEA ligands. **b,** Commercially available PC and PEA ligands. **d,** Multi-zwitterionic ligands.

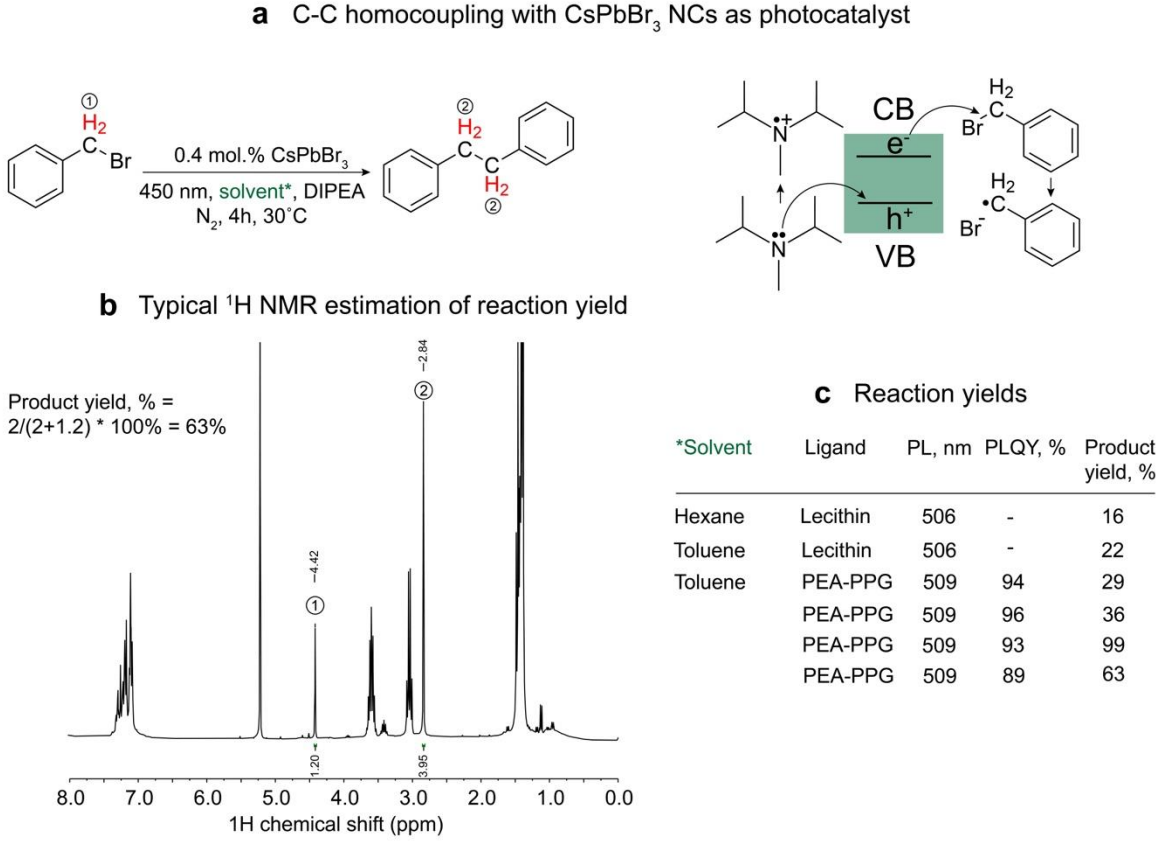

c Reaction yields

*Solvent	Ligand	PL, nm	PLQY, %	Product yield, %
Hexane	Lecithin	506	-	16
Toluene	Lecithin	506	-	22
Toluene	PEA-PPG	509	94	29
	PEA-PPG	509	96	36
	PEA-PPG	509	93	99
	PEA-PPG	509	89	63

Extended Data Fig. 7: Photocatalysis with poly(propylene glycole) PEA capped $CsPbBr_3$ NCs **a,** Photocatalytic C-C coupling reaction through activation of C-Br bond in benzyl bromide, catalyzed by $CsPbBr_3$ NCs. **b**, ^1H NMR of the final reaction mixture showing peaks from the starting material (around 4.4 ppm) and product (around 2.2 ppm) and how the reaction yield was calculated from integrating the two peaks. **c**, A table summarizing product yields in different solvents and with NCs capped with either commercial lecithin or poly(propylene glycole) (PPG)-PEA.

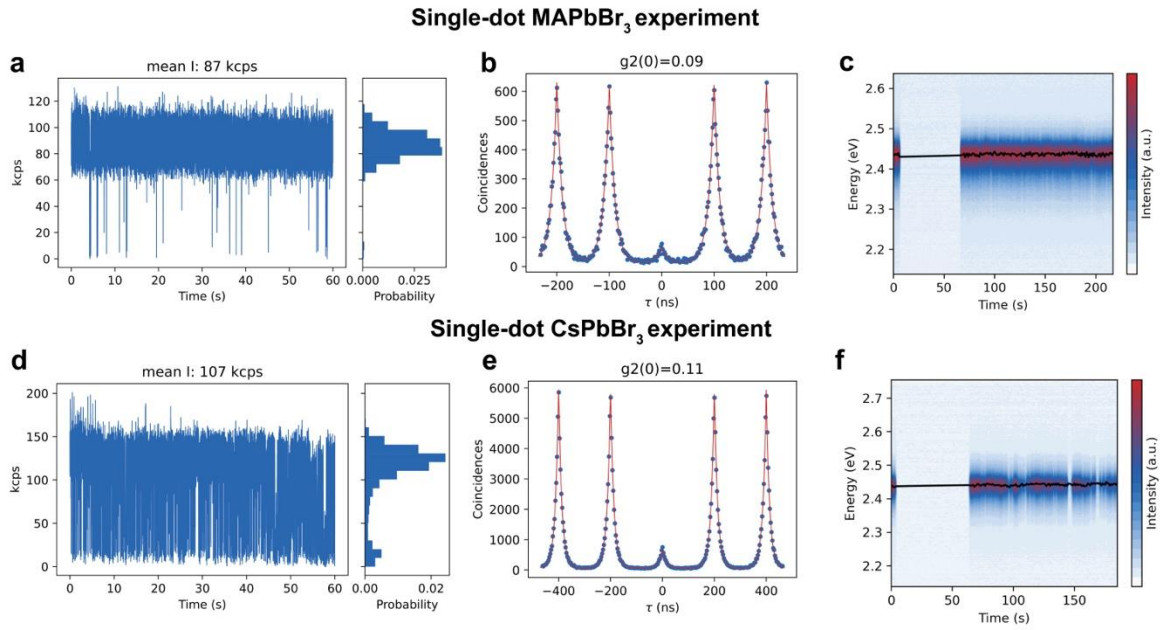

Extended Data Fig. 8: $MAPbBr_3$ and $CsPbBr_3$ single-dot emission at room temperature
These NCs were capped with C8C12-PEA-ligands and purified three times, followed by dilution ($\times 10^5$) and spin-coating onto a glass substrate. **a,d**, Blinking traces of $MAPbBr_3$ and $CsPbBr_3$ single dots. **b,e**, Pronounced antibunching evidence high purity of single photon emission. **c,f,** Stable and narrow emission from a single $MAPbBr_3$ NC (**c**) or $CsPbBr_3$ NC (**f**).

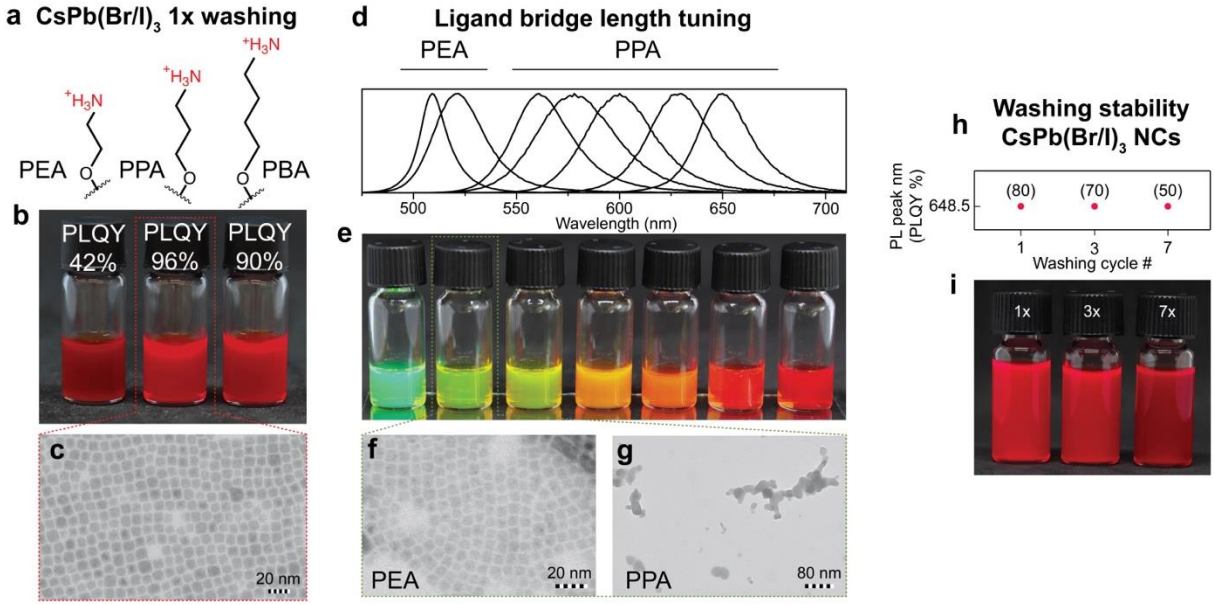

Extended Data Fig. 9: Head-group optimization by tuning the bridge length
a,b,c, Lead iodide perovskites have a larger distance between A and X surface sites than bromides. Positive-to-negative moieties distance in the zwitterion thus has a pronounced effect on the ligand binding. Mixed halide $CsPb(Br/I)_3$ NCs (without anti-solvent purification, synthesis details in **Supplementary Table 7**) capped with phosphoalkylamine ligands featuring different distances between ammonium and phosphate functionalities (**a**): PEA, PPA, and PBA. After the first purification step with anti-solvent (**b**), PEA-capped NCs

drop in PLQY from 95% to 42%, while longer-bridge PPA and PBA ligands retain high PLQY and NCs shape (**c**). **d,e,f,g**, In general, PEA ligands better suit Br-rich compositions, while PPA ligands make for a better choice for I-rich compositions. **h,i,** Mixed halide $CsPb(Br/I)_3$ NCs capped with 3-ammoniopropyl (2-octyl-1-dodecyl) phosphate (*PPA-R6*) display remarkable spectral stability during purification cycles with antisolvent (ethyl acetate:acetonitrile).

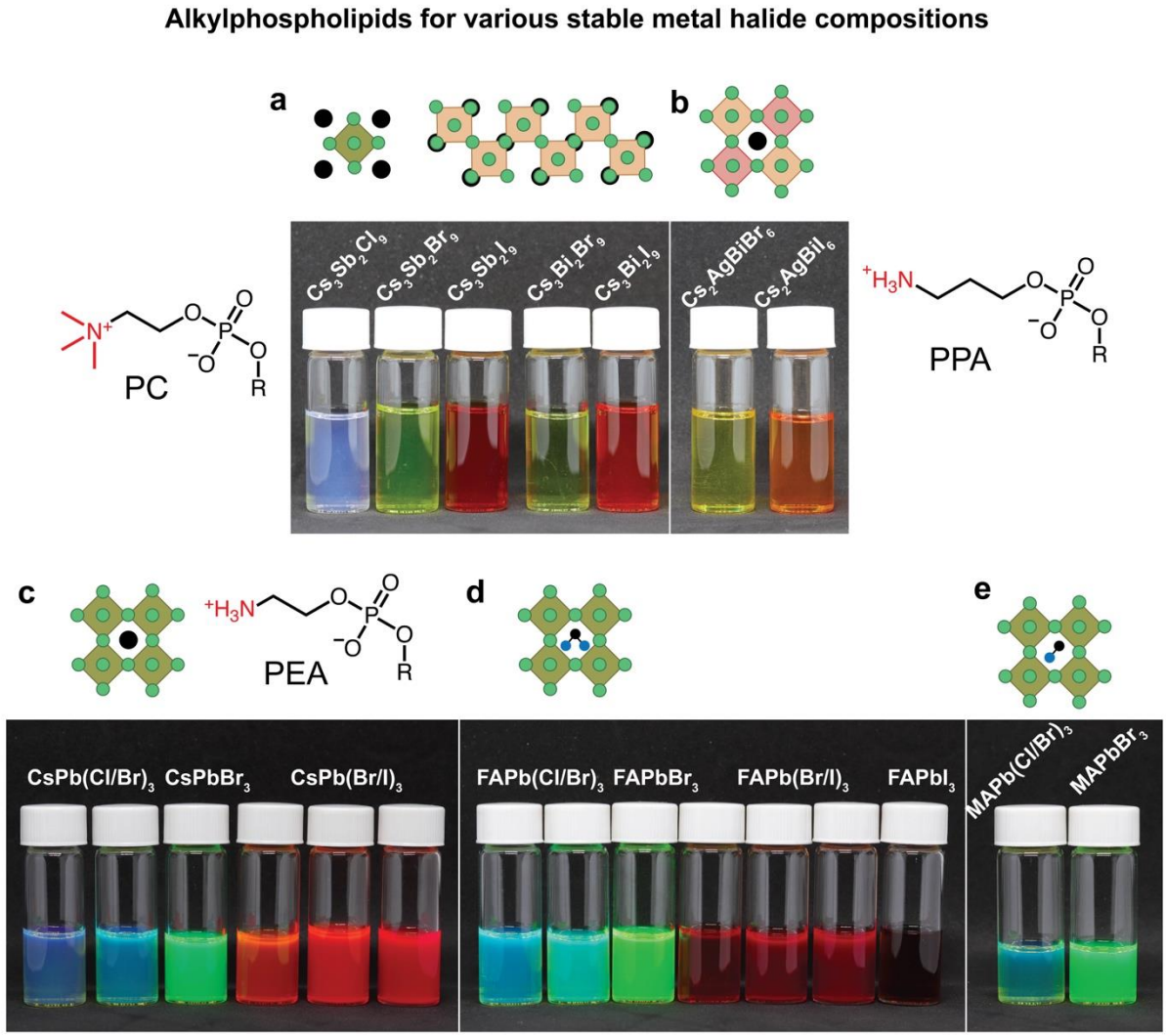

Extended Data Fig. 10: A compositional variety of metal halide NCs that can be stabilized with alkylphospholipid zwitterionic capping ligands

a,b, Lead-free metal halides: low-dimensional **(a**) or double perovskites (**b**). **c,d,e,** Stable lead halide perovskite NCs with all three cations: Cs (**c**), FA (**d**) and MA (**e**), as well as of varying halide composition, can be prepared using zwitterionic ligands with phosphate and primary ammonium head-groups and varying bridge length (PEA, PPA, PBA) (additionally see **Supplementary Figs. 15-17**).

Supplementary Files

This is a list of supplementary files associated with this preprint. Click to download.

- SupplementaryInformation.pdf